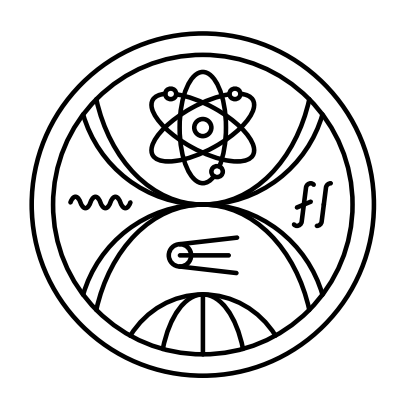
FACULTY OF MATHEMATICS, PHYSICS AND INFORMATICS

COMENIUS UNIVERSITY, BRATISLAVA



DECAY SPECTROSCOPY OF ¹⁸⁶BI AND PRODUCTION OF RADON AND RADIUM ISOTOPES

DISSERTATION THESIS

Comenius University, Bratislava Faculty of Mathematics, Physics and Informatics

DECAY SPECTROSCOPY OF ¹⁸⁶BI AND PRODUCTION OF RADON AND RADIUM ISOTOPES

DISSERTATION THESIS

Study program: Nuclear and subnuclear physics

Department: Department of Nuclear Physics and Biophysics

Supervisor: doc. Mgr. Stanislav Antalic, PhD.

Consultant: Mgr. Boris Andel, PhD.

Declaration of authorship
I hereby declare, that I personally carried out this dissertation project with help of my supervisor, consultant and with use of the listed literature and sources.
Bratislava, 2024
Adam Sitarčík

${\bf Acknowledgments}$

I would like to thank my supervisor, doc. Mgr. Stanislav Antalic, PhD. for his priceless advice, comments, support and a lot of patience. Also, I would like to thank my colleagues for many interesting discussions, help and great working environment.

Abstract:

The fusion-evaporation reactions are a great tool for the production of neutron-deficient nuclei from the lead region. The structure of nuclei from this region manifests itself via a multitude of interesting phenomena, for example nuclear isomerism, intruder states, shape coexistence and many more. In this project, the structure of 182 Tl populated after an α decay of 186 Bi (produced in the 95 Mo(93 Nb, ^{2}n) 186 Bi and 46 Ti(144 Sm, ^{2}n) 186 Bi reactions) was investigated and preliminary results are presented. Several new levels could be identified on the basis of prompt $\alpha - \gamma$ coincidences. An alternative approach considering $\alpha + e^-$ summing effects is explained and employed, by the use of which four new transitions could be tentatively assigned to the 182 Tl.

The second part of the project is aimed to investigate the production of radon and radium neutron-deficient isotopes. The main goal is to determine the fission barrier scaling parameter for each reaction, by comparing theoretical cross sections obtained with the code HIVAP with the experimental ones. The theoretical background explaining the mechanisms of the fusion-evaporation reactions and all relevant decay modes is presented.

Key words: alpha decay, decay spectroscopy, fusion-evaporation reactions, cross section

Abstrakt:

Fúzno-výparné reakcie predstavujú výborný nástroj pre produkciu neutrónovo-deficitných jadier z oblasti olova. Štruktúra jadier z tejto oblasti sa prejavuje rôznymi zaujímavými javmi, ako napríklad jadrovou izomériou, tzv. "intruder" stavmi, tvarovou koexistenciou a mnohými ďalšími. V rámci projektu bolo študované jadro 182 Tl produkované po α rozpade 186 Bi (produkovaného v reakciách 95 Mo(93 Nb, ^{2}n) 186 Bi a 46 Ti(144 Sm, ^{2}n) 186 Bi) a predbežné výsledky sú prezentované. Niekoľko nových stavov bolo identifikovaných na základe promptných $\alpha-\gamma$ koincidencií. Alternatívny prístup zohľadňujúci $\alpha-e^-$ sumácie je vysvetlený a použitý, vďaka nemu boli predbežne priradené ďalšie štyri prechody v 182 Tl.

Druhá časť projektu je zameraná na štúdium produkcie neutrónovo-deficitných izotopov radónu a rádia. Hlavným cieľom je určenie škálovacieho faktoru štiepnej bariéry pre každú študovanú reakciu, porovnaním teoretických účinných prierezov podľa kódu HIVAP s experimentálnymi hodnotami. Prezentovaný je teoretický základ popisujúci mechanizmus fúzno-výparných reakcií spolu s popisom relevantným rozpadových módov.

Kľúčové slová: alfa premena, rozpadová spektroskopia, fúzno-výparné reakcie, účinný prierez, štatistický kód

List of Abbreviations and Symbols

Z Atomic number (number of protons)

CE Conversion electron

CERN Conseil européen pour la recherche nucléaire - European organization for nuclear research

CN Compound nucleus

ER Evaporation residue

FER Fusion-evaporation reaction

FF Fission fragment

FWHM Full width at half maximum

g.s. Ground state

GSI Gesellschaft für Schwerionenforschung - Center for heavy ion research

HF Hindrance factor

IC Internal conversion

ICC Internal conversion coefficient

PSSD Position-sensitive silicon detector

QF Quasi-fission

SCC Scale Coulomb counter

SHIP Separator for heavy ion reaction products

TAC Time-to-amplitude converter

 ${f TOF}$ Time of flight

UNILAC Universal linear accelerator

Contents

Intr	oduction	1			
Obj	ectives of the dissertation thesis	5			
1.1	Production of isotopes from radon region	5			
	1.1.1 Previous studies of the cross section systematics in the lead				
	region	6			
1.2	Decay spectroscopy of ¹⁸⁶ Bi	7			
	1.2.1 Previous studies of ¹⁸⁶ Bi	7			
Phy	sical background	9			
2.1	Fusion-evaporation reactions	9			
	2.1.1 Cross section of the fusion-evaporation reaction	13			
2.2	Other types of reactions	17			
2.3	Nuclear decays	17			
	2.3.1 Alpha decay	18			
	2.3.2 Internal transitions	21			
2.4	Nuclear isomerism	28			
Experimental Background 3					
3.1	Experimental production of nuclei	31			
3.2	Nuclei separation - SHIP	32			
3.3	Detector system	34			
	3.3.1 Calibrations	38			
3.4	Methods for nuclear structure studies	38			
	3.4.1 Decay spectroscopy	38			
	3.4.2 Other methods	38			
3.5	Data analysis	38			
	3.5.1 Electronics and signal processing	38			
	Obj 1.1 1.2 Phy 2.1 2.2 2.3 2.4 Exp 3.1 3.2 3.3 3.4	1.1.1 Previous studies of the cross section systematics in the lead region 1.2 Decay spectroscopy of ¹⁸⁶ Bi 1.2.1 Previous studies of ¹⁸⁶ Bi Physical background 2.1 Fusion-evaporation reactions 2.1.1 Cross section of the fusion-evaporation reaction 2.2 Other types of reactions 2.3 Nuclear decays 2.3.1 Alpha decay 2.3.2 Internal transitions 2.4 Nuclear isomerism Experimental Background 3.1 Experimental production of nuclei 3.2 Nuclei separation - SHIP 3.3 Detector system 3.3.1 Calibrations 3.4 Methods for nuclear structure studies 3.4.1 Decay spectroscopy 3.4.2 Other methods 3.5 Data analysis			

CONTENTS CONTENTS

		3.5.2	Time-position correlation technique	40
		3.5.3	Statistical analysis in case of poor statistics	42
4	Res	ults an	d discussion	47
	4.1	Produc	ction of isotopes from radon region	48
		4.1.1	Reactions leading to radon compound nuclei	48
		4.1.2	Reactions leading to a tatine compound nuclei	51
		4.1.3	Barrier-scaling systematics	51
	4.2	Decay	spectroscopy of ¹⁸⁶ Bi	53
		4.2.1	Experimental details	53
		4.2.2	Results and discussion	53
5	Sun	nmary		59
Aı	ppen	dices		case of poor statistics 42 47 48 adon region 48 adon compound nuclei 51 statine compound nuclei 51 atics 53 53 53 53 53 compound nuclei 63
\mathbf{A}	Exc	itation	functions for radon compound nuclei	63
В	Exc	itation	functions for a tatine compound nuclei	67

Introduction

Even after more than 100 years since the discovery of the atomic nucleus by E. Rutherford in 1911 [Rut11], the nuclear structure still draws many questions and presents itself in various, often unexpected ways. The vicinity of the closed proton nuclear shell at Z=82 is especially rich in these manifestations of the nuclear structure, for example, nuclear isomerism (first observed by Otto Hahn in ²³⁴Pa [Hah21]), double and triple shape coexistence, first observed in ¹⁶O [Mor56] and in ¹⁸⁶Pb [And00], respectively, or the exotic decay modes such as β -delayed fission [Kuz67a; Kuz67b].

For the production of exotic nuclei, two methods are widely used. The isotope separation online (ISOL) method uses the bombardment of a thick target by high-energy particles, resulting in spallation, fission, or fragmentation of the target nuclei. One of the most successful facilities employing this method is ISOLDE [Kug00] in CERN, Geneva. The second method of fusion-evaporation reactions uses the bombardment of thin a target with low-energy projectiles. Reaction products leaving the target are separated by gas-filled or vacuum-mode separators, such as the velocity filter SHIP [Mün79], in GSI, Darmstadt.

The first part of the dissertation thesis is the investigation of the ¹⁸⁶Bi isotope and its α -decay daughter product ¹⁸²Tl with the use of $\alpha - \gamma$ decay spectroscopy. The studies of thallium and bismuth isotopes in the neutron-deficient side of the nuclide table revealed a multitude of phenomena linked to the near vicinity of the proton closed shell Z = 82. A systematic appearance of low-lying intruder states is ranked among the most interesting ones [Hey83; Hey87; Hey88; Woo92]. The $1/2^+$ ground state in the odd-mass thallium nuclei is caused by the valence $3s_{1/2}^{-1}$ proton $\pi(0p-1h)$ configuration, while the the low-lying intruder $9/2^-$ state with $\pi(1p-2h)$ configuration is caused by the excitation of a proton across the Z = 82 gap to the $1h_{9/2}$ orbital. The situation in the even-mass thallium and bismuth nuclei is much more complex, due to the additional coupling of an unpaired neutron resulting in

the multiplets of states. The multiplets can be both normal or intruder and can become isomeric states as well. A relatively small energy difference between the multiplets and/or the collective bands built on top of them can further complicate the studies.

Previous analysis of the 95 Mo(93 Nb, 2n) 186 Bi [And03] and 97 Mo(92 Mo,p2n) 186 Bi [Bat97] reactions revealed two isomeric states in 182 Tl populated after an α decay of 186 Bi with very similar half-lives. Only three γ transitions were identified in the former study and assigned to these isomers based on the energy balance of the observed transitions. Several other γ transitions remained unresolved and were not assigned to either of the isomers.

Data from the reaction $^{46}\text{Ti}(^{144}\text{Sm}, p3n)^{186}\text{Bi}$ measured at the velocity filter SHIP, Darmstadt, are available. A merger of the datasets from this and the aforementioned $^{95}\text{Mo}(^{93}\text{Nb}, 2n)^{186}\text{Bi}$ reactions increased the statistics of the collected data from the decay of ^{186}Bi about three times. The increased statistics allow us to extend the decay scheme and assign almost the entire spectrum of the γ transitions following the α decay of ^{186}Bi with the use of prompt α - γ coincidences.

The effects of unpaired nucleons can be seen in the spectra of 186 Bi α -decay energies populating certain levels in 182 Tl. De-excitation transitions can be heavily converted and the α -decay energies may be summed up with the energies of the conversion electrons. The α -decay energy distributions corresponding to such γ transitions may be difficult to disentangle and interpret. The analysis of such distributions and an alternative interpretation of the excited states within 182 Tl will be described and employed.

The second aim of the project is the investigation of the cross section systematics in the fusion-evaporation reactions leading to neutron-deficient compound nuclei from the radon region. Investigation of rare and exotic demonstrations of the nuclear structure requires large amounts of collected data, often in millions of registered decays. However, the production of the neutron-deficient nuclei far away from the line of β -stability reaches its limits, thus reliable theoretical models predicting the yields of the measured reactions are crucial.

Nowadays, one of the most widely used models to estimate the cross sections of the fusion-evaporation reactions is the statistical code HIVAP [Rei81; Rei92]. As has been shown in recent years, one of the parameters entering the calculation, the fission barrier, is heavily reduced in the reactions leading to the neutron-deficient compound nuclei in the vicinity of the closed proton shell Z = 82 [And05]. The

decrease of the barrier by around 30% causes the cross section to drop by several orders of magnitude. The dependence of the fission barrier scaling factor and mass of the compound nucleus is known from the bismuth and polonium neutron-deficient isotopes.

A smaller but still very significant decrease of the fission barrier is expected in radon and radium compound nuclei (around 27% for ¹⁹⁹Rn*, according to the mentioned systematics). However, up to this day, no analysis focused on the evaluation of the cross sections in this region has been performed. Currently, data from the reactions leading to the neutron-deficient radon and radium isotopes are available. The reactions were measured at several projectile energies, which allows the establishment of the corresponding excitation functions. Through the variation of the parameters entering the theoretical calculation, the predictions will be varied to fit the experimental results and the optimal set of the parameters will be extracted. One of these parameters, the aforementioned fission barrier scaling factor, will help to extend the systematics known from the polonium and bismuth isotopes.

The first chapter is dedicated to the theory behind the fusion-evaporation reactions and decays analyzed in the project - alpha decay, gamma decay, and internal conversion. The details about the experimental setup - velocity filter SHIP and the detector system - are listed in the second chapter. The electronics and signal processing are presented therein, together with the description of the time-position correlation technique and the statistical analysis in case of poor statistics. The third chapter lists the goals and summary of previous studies concerning the main aims of the project. In the fourth chapter, preliminary results from the $\alpha - \gamma$ analysis of the decay data of ¹⁸⁶Bi are presented. The sixth chapter contains a summary of the results and outlook.

Chapter 1

Objectives of the dissertation thesis

In this chapter main aims of the dissertation thesis will be presented. The thesis is divided into two parts:

- Study of production systematics in the reactions leading to compound nuclei from the neutron-deficient region around Z=86
- Decay spectroscopy of 186 Bi and its α -decay product 182 Tl

For each part, the previous studies on the topic are summarized.

1.1 Production of isotopes from radon region

Data from the $^{52}\text{Cr}+^{147,149,150}\text{Sm} \rightarrow ^{199,201,202}\text{Rn}^*$ and $^{56}\text{Fe}+^{147,149,154}\text{Sm} \rightarrow ^{203,205,210}\text{Ra}^*$ reactions measured at the SHIP are available.

I'll add also astatine CNs

The main aim is to obtain experimental cross sections of the reaction products for different reactions and compare them with the theoretical calculations according to the statistical code HIVAP (section 2.1.1). By optimizing the theoretical predictions to reproduce the experimental values, an optimal fission barrier scaling parameter will be extracted.

More specifically, the completion of the following goals is expected:

• Calibration of the detector setup for each reaction: calibration of PSSD with use of known α peaks; calibration of the γ detector with a use of 152 Eu; determination of the efficiency curve of the γ detector.

- Identification of the produced isotopes based on known α energies and halflives. The isotopes with similar α decay energies will be differentiated based on the α - γ coincidence analysis. Alternatively, the use of the correlation technique can be employed, however, relatively long half-lives of the expected reaction products could be a limiting factor.
- Evaluation of the experimental cross sections and of the corresponding statistical uncertainties.
- Theoretical calculations of the excitation functions via the code HIVAP the variation of the fission barrier scaling parameter will allow to fit the experimental values. The decrease of the parameter in the compound nucleus ²⁰²Rn by around 27% is expected (according to the systematics from [And05]). Additionally, the theoretical cross sections can be evaluated by alternative approaches and models, such as Nuclear Reaction Video (NRV) calculation [Kar17] or the evaluation by the software LISE++ [Tar08], and compared with the HIVAP.
- Extraction of the optimal scaling parameter value for each analyzed reaction will allow the extension of the known systematics by astatine, radon, and radium compound nuclei.

1.1.1 Previous studies of the cross section systematics in the lead region

The production of the neutron-deficient polonium and bismuth isotopes was studied by using FERs measured at the SHIP, GSI. The cross sections of the xn and pxn evaporation channels in the reactions $^{46}\text{Ti}+^{144}\text{Sm}\rightarrow^{190}\text{Po}^*$, $^{98}\text{Mo}+^{92}\text{Mo}\rightarrow^{190}\text{Po}^*$, $^{50,52}\text{Cr}+^{142}\text{Nd}\rightarrow^{192,194}\text{Po}^*$ and $^{94,95}\text{Mo}+^{93}\text{Nb}\rightarrow^{187,188}\text{Bi}^*$ were evaluated. The experimental results together with known cross section data for the other heavier polonium and bismuth isotopes were compared with the theoretical calculations obtained from the statistical model HIVAP (section 2.1.1) [And05].

The parameters entering the theoretical calculations had fixed values corresponding to the studied reaction. The only free parameter of the calculation was the scaling factor of the liquid-drop model fission barrier. To reproduce the experimental data with the theoretical calculations, the decrease of the fission barrier by a factor of up to 35% was required. The difference between the theoretical cross sections

calculated with such a scaled barrier and unscaled one can reach up to three orders of magnitude.

1.2 Decay spectroscopy of ¹⁸⁶Bi

The main aim is to analyze the structure of 182 Tl, produced as an α decay product of 186 Bi, via $\alpha - \gamma$ coincidence analysis. Currently, data from the reactions 46 Ti+ 144 Sm and 95 Mo+ 93 Nb (already analyzed in [And03]) measured at the SHIP are available, the merger of the datasets increased the total number of 186 Bi collected almost three times in comparison with the analysis in the reference. The statistics increase allows to assign the majority of γ signals in coincidences with α decays originating from either isomer in 186 Bi.

More specifically, the completion of the following goals is expected:

- Calibration of the detector setup: calibration of PSSD with a use of known α peaks; calibration of the γ detector with a use of 152 Eu; determination of the efficiency curve of the γ detector.
- Identification of the produced nuclei.
- Determination of the half-lives of both ¹⁸⁶Bi isomers, to verify the previously determined value from [Bat97; And03].
- Analysis of the $\alpha \gamma$ coincident spectra, with an emphasis on the γ lines coincident with the α decay of ¹⁸⁶Bi. The $Q(\alpha) + E_{\gamma}$ value for each $\alpha \gamma$ group will be determined, along with the corresponding half-lives extracted from the $ER (\alpha \gamma)$ correlation search.
- In case of the complex α distributions of $\alpha \gamma$ groups, which will indicate $\alpha + CE$ summing effects, the tentative determination of the converted transitions their energy and multipolarity will be performed.
- $\bullet\,$ The decay scheme of $^{186}{\rm Bi}$ and of the states in $^{182}{\rm Tl}$ will be constructed.

1.2.1 Previous studies of ¹⁸⁶Bi

Alpha decay activity of 186 Bi was first observed by J. R. H. Schneider [Sch84b]. He reported one 7191(25) keV α activity with a half-life of 10(4) ms.

Further study conducted by J. C. Batchelder [Bat97] examined ¹⁸⁶Bi produced in a ⁹⁷Mo(⁹²Mo, p2n) reaction. Two α activities correlated with α particles from the α decay of ¹⁸²Hg (produced by β^+ /EC of ¹⁸⁶Bi α -decay daughter product, ¹⁸²Tl) were observed - 7158(20) keV with $T_{1/2} = 15.0(17)$ ms a 7261(20) keV with $T_{1/2} = 9.8(13)$ ms. Higher energy (shorter-lived) activity was assigned to (10⁻) and lower energy (longer-lived) activity was assigned to (3⁺) isomeric state in ¹⁸⁶Bi, based on the systematics from [Van91] aimed on the investigation of heavier odd-odd bismuth isotopes (^{190–196}Bi) and due to higher intensity of 7261 keV α line (since higher spin states are expected to be populated preferentially).

The later study [And03] investigated ¹⁸⁶Bi produced in the ⁹⁵Mo(⁹³Nb, 2n)¹⁸⁶Bi complete fusion reaction measured at the SHIP, GSI at 419 and 438 MeV beam energies in front of the target. The collected statistics was around 50 times greater than in the previous studies, which allowed the measurement of coincident γ rays after α decay of ¹⁸⁶Bi and provided more detailed information about the nuclide. The study reported two α activities (similarly to [Bat97]), with 7261(20) keV and 7152(15) keV energies and 9.8(4) ms and 14.8(8) ms half-lives, denoted as ^{186m1}Bi and ^{186m2}Bi, respectively¹. Based on the $\alpha - \gamma$ coincidence analysis and $Q(\alpha) + E_{\gamma}$ summing, 7080-520 and 7152-444 keV $\alpha - \gamma$ groups were assigned to the ^{186m2}Bi isomer and 7263-108.5 keV was assigned to the ^{186m1}Bi. The most intense, 108.5 keV γ transition was assigned E1 multipolarity based on the GEANT4 Monte Carlo simulations. Other $\alpha - \gamma$ groups were not assigned due to low statistics, $\alpha - e^{-}$ summing effects emerging from the internal conversion and similar half-lives of both isomers. Direct, full energy crossovers of either isomer were not observed or could not be resolved.

¹This notation will be used throughout the work.

Chapter 2

Physical background

2.1 Fusion-evaporation reactions

To this date, fusion-evaporation reactions (FER), which are also referred to as reactions of complete fusion or compound nucleus reactions, continue to be the sole method for producing nuclei that are much heavier than the ones involved in the reaction. The concept of the compound nucleus model was initially presented by N. Bohr in 1936 [Boh36] and subsequently enhanced by V. F. Weisskopf and D. H. Ewing in 1940 [Wei40].

During fusion-evaporation reactions, a projectile a with a kinetic energy¹ T_p , surpasses the fusion (Coulomb) barrier to merge with a target nucleus A. Once inside the target nucleus, the projectile's energy is distributed among all nucleons through two-body interactions until equilibrium is achieved. The result of this process is the formation of a compound nucleus (CN) characterized by high excitation energy (ranging from 20 to 60 MeV) and significant angular momentum $(60 - 80 \,\hbar)$. The compound nucleus is typically created in a time frame of around 10^{-22} s [Lov06]. If the excitation energy of the a + A system significantly exceeds the fission barrier, quasi-fission (QF) can occur. Write more about QF, explain du Rietz's paper about quasi-fission, explain the equations for fissilities which were used in it and show the fig. with systematics in respect to fissilities, maybe mention the extent to which the systematics hold true.

The excessive excitation energy of the compound nucleus is radiated in the form of nucleons and/or α particles within a timespan of approximately 10^{-19} – 10^{-16} s. The deexcitation process of the excited compound nucleus is analogous to the evaporation

¹All kinetic energies are in the laboratory frame throughout the work, unless stated otherwise

of molecules from a hot liquid. The number of evaporated particles depends on the excitation energy, and the emission of each particle cools down the compound nucleus by roughly 10 MeV. Neutron evaporation channels (xn), where x denotes the number of evaporated neutrons) are usually predominant. In the neutron-deficient region, proton (pxn) channel, involving one proton and x neutrons) and/or α (αxn channel, comprising one α particle and x neutrons) emission becomes favored due to the increase in neutron binding energies and a simultaneous decrease in proton binding energies.

The evaporation of a nucleon results in a relatively small reduction in angular momentum. If further nucleon evaporation would lead to states below the state of the nucleus with the minimal possible angular momentum for the given excitation energy (yrast line), further de-excitation occurs through discrete γ transitions. This process forms a yrast cascade, as illustrated in Fig. 2.1 and typically occurs over the interval of about $10^{-17} - 10^{-10} \,\mathrm{s}$. The final de-excited product in the ground or isomeric state is referred to as an evaporation residue (ER).

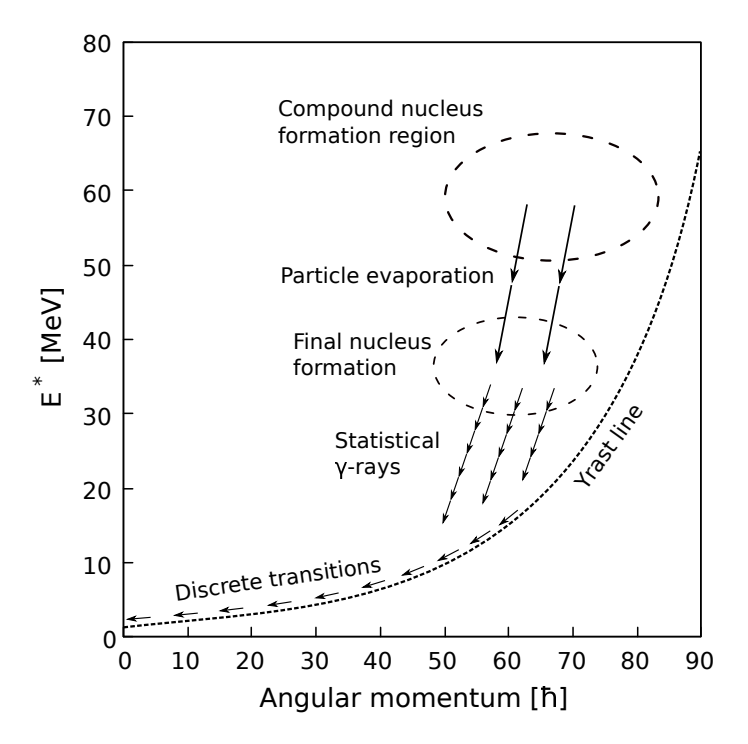


Figure 2.1: Process of particle and γ evaporation from the excited compound nucleus.

The process of the fusion-evaporation reactions can be schematically written as:

$$a + A \rightarrow CN^* \rightarrow B + b$$

where B represents evaporation residue and evaporated particles are stated as b. Simplified notation of the reaction is A(a,b)B. A visual representation of the process is in Fig. 2.2.

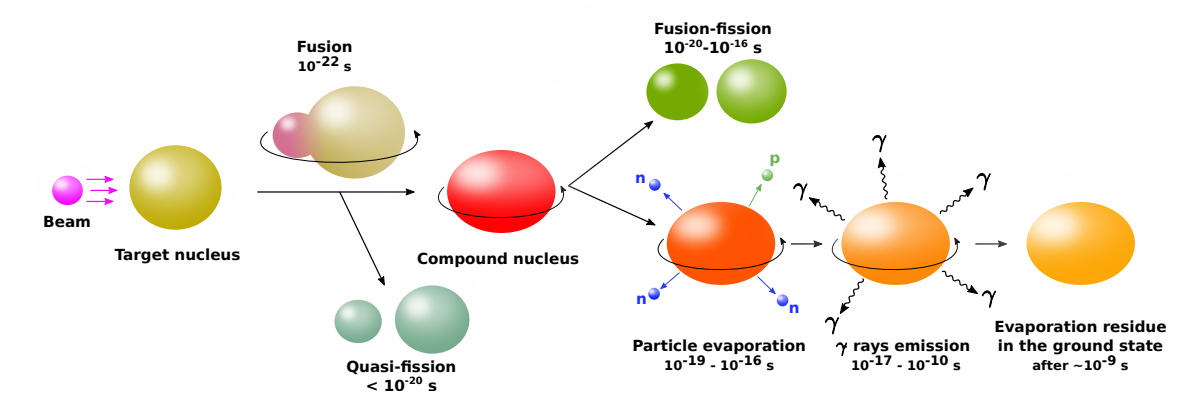


Figure 2.2: Visualisation of the process of fusion-evaporation reactions.

The energy balance of the reaction can be expressed via the masses of a projectile m_p , a target m_T , and an excited compound nucleus m_{CN}^* and kinetic energies of the projectile T_p , and the CN T_{CN} :

$$(m_p + m_T)c^2 + T_p = m_{CN}^*c^2 + T_{CN}$$
(2.1)

Since the momentum of the projectile $|\overrightarrow{p_p}|$ is equal to the momentum of the CN $|\overrightarrow{p_{CN}}|$ (conservation of momentum), the kinetic energy of the CN can be expressed as

$$T_{CN} = \frac{p_{CN}^2}{2m_{CN}^*} = \frac{m_p}{m_p} \frac{p_{CN}^2}{2m_{CN}^*} = \frac{m_p}{m_{CN}^*} \frac{p_p^2}{2m_p} = \frac{m_p}{m_{CN}^*} T_p$$
 (2.2)

Combining equations 2.1 and 2.2, the expression for the mass of the excited CN is

$$m_{CN}^*c^2 = (m_p + m_T)c^2 + T_p \left(1 - \frac{m_p}{m_{CN}^*}\right)$$
 (2.3)

An approximation $m_{CN}^* = m_p + m_T$ can be done for $m_{CN}^* >> m_p$. Then

$$m_{CN}^*c^2 = (m_p + m_T)c^2 + T_p\left(1 - \frac{m_p}{m_p + m_T}\right) = (m_p + m_T)c^2 + T_p\left(\frac{m_T}{m_p + m_T}\right)$$
 (2.4)

and the excitation energy of the CN is

$$E_{CN}^* = (m_{CN}^* - m_{CN})c^2 = (m_p + m_T - m_{CN})c^2 + T_p \left(\frac{m_T}{m_p + m_T}\right)$$
(2.5)

The term $(m_p + m_T - m_{CN})c^2$ represents the Q value of the reaction and comes from the difference of binding energies. The kinetic energy of the projectile is represented by the $T_p m_T / (m_p + m_T)$ term.

The energy spectrum of the evaporated neutrons shown in Fig. 2.3 can be expressed as

$$N(\varepsilon) d\varepsilon = \frac{\varepsilon}{T^2} \exp\left(\frac{-\varepsilon}{T}\right) d\varepsilon$$
 (2.6)

where the nuclear temperature T is given by

$$E^* = aT^2 - T \tag{2.7}$$

The excitation energy of the nucleus is E^* and a is the level density parameter A/12 - A/8 from the Fermi gas model [Lov06].

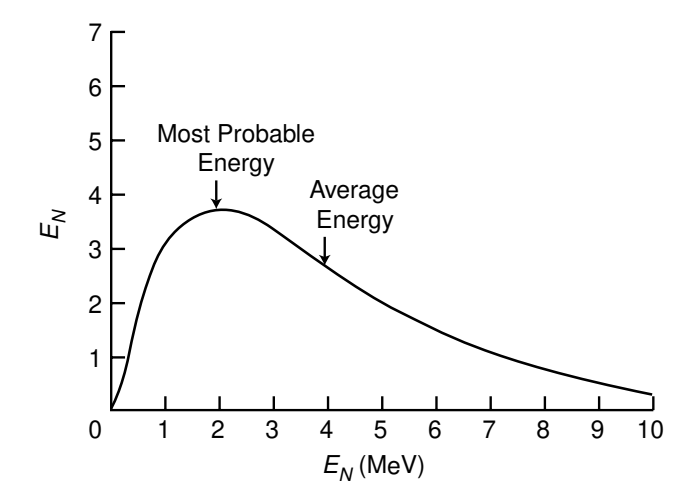


Figure 2.3: The energy spectrum of the neutrons emitted from the excited compound nucleus [Lov06].

The most probable energy of the neutrons is denoted as T, while the average energy is twice that value, 2T. Unlike the evaporation of neutrons, the evaporation of a charged particle (such as a proton or an alpha particle) requires a non-zero kinetic energy, denoted as ε_s . This kinetic energy determines the minimum energy threshold for the particle. In essence, this threshold energy is approximately equal to the Coulomb barrier. The energy spectrum of the evaporated charged particles can then be described by the equation:

$$N(\varepsilon) d\varepsilon = \frac{\varepsilon - \varepsilon_s}{T^2} \exp\left(\frac{-\varepsilon - \varepsilon_s}{T}\right) d\varepsilon$$
 (2.8)

2.1.1 Cross section of the fusion-evaporation reaction

A significant characteristic of these reactions is that the probability of producing a specific evaporation residue (cross section of the reaction) is independent of how the compound nucleus was formed. This hypothesis, also known as the Bohr independence hypothesis or the amnesia assumption, was experimentally confirmed by S. N. Ghoshal [Gho50]. In the experiment, the compound nucleus 64 Zn* was produced in two reactions, 63 Cu+p and 60 Ni+ α . The ratios between the cross sections $\sigma(\alpha,n):\sigma(\alpha,2n):\sigma(\alpha,pn)$ for the 60 Ni target were found to be consistent with those of $\sigma(p,n):\sigma(p,2n):\sigma(p,pn)$ for the 63 Cu target. The excitation functions, which illustrate the dependence of the reaction cross section on the excitation energy of the compound nucleus or the energy of the incident projectile, are depicted in Figure 2.4.

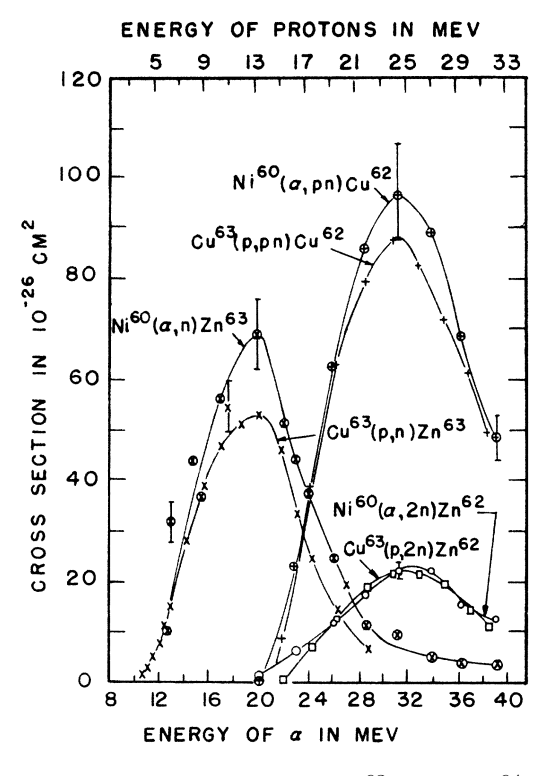


Figure 2.4: Experimental excitation functions of $^{63}\text{Cu} + p \rightarrow ^{64}\text{Zn}^*$ and $^{60}\text{Ni} + \alpha \rightarrow ^{64}\text{Zn}^*$ reactions from [Gho50]

The independence of the entrance and exit channels of the FERs allows us to express the cross section of $a + A \rightarrow CN^* \rightarrow b + B$ reaction as

$$\sigma(a,b) = \sigma_{CN}(a,A)P_b(E)$$
(2.9)

where $\sigma_{CN}(a, A)$ represents the cross section (probability) of the creation of the compound nucleus and $P_b(E)$ is the probability that CN with excitation energy E decays by evaporation of particle(s) b.

Experimental cross section

The total number of ERs produced in the reaction (N_{Re}) is proportional to the cross section of the reaction (σ) , the number of the projectiles (N_p) , and the area density of the nuclei in the target per area unit (η) :

$$N_{ER} = \sigma N_p \eta \tag{2.10}$$

where area density is expressed as

$$\eta = f \frac{N_T}{S} \tag{2.11}$$

The parameter f is the ratio of desired target nuclei to the total number of nuclei in the target (known as the isotopic purity) and N_T is the number of target nuclei with an area S. Further, $N_T = \frac{m}{M_m} N_A$ where m is the mass of the target, M_m is the molar mass of the target nuclei and N_A is the Avogadro constant.

The number of observed decays N_i originating from the ERs is lower than the total number of ERs produced in the reaction. Detector efficiency ε_i for the detected particles (see section 3.3), transmission of the SHIP separator ε (see section 3.2 and Fig. 3.3) and branching ratio of the corresponding decay must be considered as well. Relation between N_{ER} and N_i is

$$N_i = b_i \varepsilon_i \varepsilon N_{ER} \tag{2.12}$$

The total number of ERs produced in the reaction is then

$$N_{ER} = \sigma N_p f \frac{N_T}{S} = \sigma N_p f \frac{m}{S} \frac{N_A}{M_m} = \sigma N_p f d \frac{N_A}{M_m} = \frac{N_i}{b_i \varepsilon_i \varepsilon}$$
 (2.13)

where d = m/S is the width of the target in g/cm² and M_m/N_a represents an atomic mass of the target nucleus.

The total number of projectiles is derived from the charge collected by a Faraday cup Q divided by the charge state of the projectiles q and elementary charge e. The total collected charge can be expressed in terms of the total charge collection time t and an average beam current \overline{I} or a beam current during the pulse I and the duty

factor D, reflecting pulse-regime of the accelerator (as a ratio between a pulse time and a total macropulse duration):

$$N_p = \frac{Q}{qe} = \frac{\overline{I}t}{qe} = \frac{IDt}{qe}$$
 (2.14)

In the experiments performed at the SHIP, the beam intensity is measured in Scale Coulomb Counter units (SCC). The value of beam current changes throughout the experiment, therefore SCC unit and the SCC counting rate R is used. Charge collection time t is then given as

$$t = \frac{SCC}{R} \tag{2.15}$$

and the total number of projectiles can be expressed as

$$N_p = SCC \frac{ID}{Rqe} \tag{2.16}$$

Finally, from the combination of equations 2.13 and 2.16, the experimental cross section of the reaction is

$$\sigma = \frac{1}{fd} \frac{M_m}{N_A} \frac{N_i}{b_i \varepsilon_i \varepsilon} \frac{R}{SCC} \frac{qe}{ID}$$
(2.17)

Statistical code Hivap

Firstly introduced by W. Reisdorf [Rei81; Rei92] as a modification of the GROGI code [Gro67]—fission channel was incorporated into the de-excitation phase of the FER. The fusion cross section is calculated via the summation of the partial waves as follows

$$\sigma_{fus}(E) = \pi \lambda^2 \sum_{l=0}^{L_{crit}} (2l+1) T_l(E)$$
 (2.18)

where λ is the reduced wavelength of the entrance channel and $T_l(E)$ are the transmission coefficients of the penetrating waves. The critical value L_{crit} of the angular momentum quantum number l emerges from the rapid decrease of the survival probability of the CN with increasing angular momentum. The typical values are $L_{crit} \sim 20$ for mercury (Z = 80) and up to $L_{crit} \sim 30$ for radium isotopes (Z = 88) [Qui93].

In the presented study, two different models are utilized to determine the values of $T_l(E)$. The first model, referred to as the inverted-parabola approach, approximates

the Coulomb plus nuclear force near its maximum using a parabola with a curvature of $\hbar\omega_l$ and a height of B_l [Vaz81]. The transmission coefficients can then be obtained from the Hill-Wheeler formula [Hil53]:

$$T_l(E) = \frac{1}{1 + \exp\left[(2\pi/\hbar\omega)(B_l - E)\right]}$$
(2.19)

The IP approach has been found to be effective above the semi-empirical Bass barrier [Bas77; Bas80], while fusion below the barrier is significantly suppressed. To account for the sub-barrier fusion, an alternative approach known as barrier-fluctuations is employed. In this approach, the fusion barrier is considered to fluctuate with a Gaussian distribution characterized by a height of B_0 and a standard deviation of $\sigma(B_0)$. The values of the barrier fluctuation are discussed in [Qui93] (see Fig. 12 and the accompanying description), where values of 2.5 and up to 3.5 are used for spherical and deformed compound nuclei, respectively. Both the barrier-fluctuations and inverted-parabola approaches have been shown to accurately reproduce cross section values above the fusion barrier as well [And05].

Table 2.1: Values of HIVAP parameters used throughout this work, majority according to [Rei90]. Parameters used with values equal to zero are not listed.

Parameter	Description	Value
LEVELPAR	Scale parameter for the level density	1.16
a_f/a_n	Level density ratio	1
BARFAC	Fission barrier scaling	variable
EDAMP	Shell effect damping constant [MeV]	18.5
V0	Strength parameter of nuclear potential [MeV]	59
R0	Radius parameter [fm]	eq. 15 in [Rei85]
D	Diffuseness parameter [fm]	0.75
Q2	Quadrupole moment of target nucleus [fm ²]	β_2 from [Möl16]
CRED	RED Barrier thickness parameter	
SIGR0	Barrier fluctuation $\sigma(B_0)$ [% of R0]	~ 2.5 for spherical nuclei
		$\lesssim 3.5$ for deformed nuclei

The de-excitation part of the calculation employs the evaporation theory and considers the competition between fission, γ ray, α -particle, and nucleon emission. The ratio of nuclear level densities (a_f/a_n) is calculated as described in [Rei92]. The

damping constant is used to represent the fading of the shell effects on the level density [Ign75]. Another crucial parameter, the fission barrier, is calculated using the following equation:

$$B_f = BF \times B_f^{RLD} - \Delta W_{gs} \tag{2.20}$$

where BF is a free scaling parameter and B_f^{RLD} is the fission barrier according to the rotating liquid drop model [Coh74]. The ground state correction $\Delta W_{gs} = M_{exp} - M_{LD}$ represents the difference between the experimental and theoretical masses from the liquid-drop model. The values of the HIVAP parameters used in the calculations are summarized in Table 2.1. ADD FEW SENTENCES ABOUT THE 'FREEDOM' OF BF PARAMETER - HOW IT IS ESSENTIALLY THE ONLY FREE PARAMETER, HOW IT INFLUENCES THE RESULTS (OTHER PARAMETERS SUCH AS SIGRO AFFECT ONLY THE SUBBARRIER PART, AND EVEN THEN, NOT DRAMATICALLY ETC.), WHY WE THINK IT IS 'PHYSICALLY' VALID THING TO SCALE THE BARRIER (RESULTS FROM OTHER METHODS WHICH SUGGEST THE SAME REDUCTION - VESEL-SKY'S 210RN, MAYBE FIND SOMETHING ELSE), HOW IT CAN POINT TO QUASI-FISSION, ALBEIT INDIRECTLY.

2.2 Other types of reactions

transfer, spallation,

2.3 Nuclear decays

The stability of atomic nuclei is characterized by an equilibrium between the number of protons and neutrons. To date, out of approximately 3300 known nuclides only 252 have never been observed to decay and are therefore considered stable. The unstable nuclei can decay either by β decay—a proton is transformed into a neutron or vice versa, or directly emitting protons, neutrons, α particles or by fission. Less common decays are, for example, double β /electron capture decays, β -delayed fission, cluster emission, and others. Studying the decay modes and their characteristic properties gives valuable information about the nuclear structure and the forces acting within the nuclei. In this section, we will provide a detailed explanation of the decays relevant to this work.

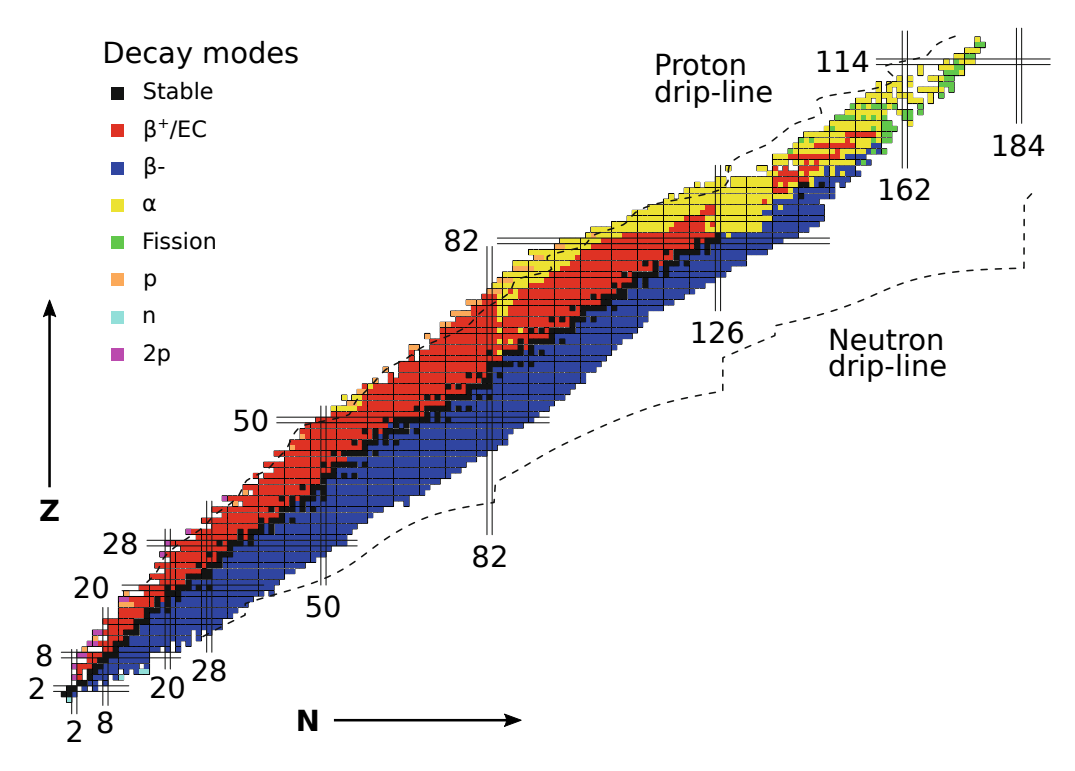


Figure 2.5: Nuclear chart showing experimentally observed nuclei. Figure adapted and modified from Ref. [Tan23].

2.3.1 Alpha decay

Alpha decay occurs when the Coulomb force, which increases with the squared atomic number of a nucleus ($\sim Z^2$), overcomes the attractive nuclear force, which increases with the mass of a nucleus ($\sim A$). Such unbalance leads to the emission of an α particle (helium nucleus), consisting of two protons and two neutrons strongly bound together. In heavy nuclei, α decay becomes energetically possible and it is the preferred mode of decay. The process of an α decay in a nucleus with mass number A, atomic number Z, and neutron number N can be represented schematically as

$${}_{Z}^{A}X_{N} \longrightarrow {}_{Z-2}^{A-4}Y_{N-2}^{2-} + {}_{2}^{4}\mathrm{He}^{2+} + Q_{\alpha}$$
 (2.21)

where Q_{α} represents the energetic balance of the reaction and can be expressed in terms of binding energies B as

$$Q_{\alpha} = \left[B\left(\begin{smallmatrix} A-4\\ Z-2 \end{smallmatrix} \right) + B(\alpha) \right] - B\left(\begin{smallmatrix} A\\ Z \end{smallmatrix} \right) \tag{2.22}$$

The Q_{α} value is positive (exothermic) for spontaneous α decay and typically ranges from around 4 up to 12 MeV. The energy released in a decay is transformed

into the kinetic energies of the daughter nucleus $(E_D, \text{ also referred to as the recoil})$ energy) and the escaping α particle (E_α) . The nuclear mass of a nucleus is $M({}_Z^AX) = Zm_p + Nm_n - B({}_Z^AX)$, therefore the Q value of an α decay can be expressed in terms of nuclear masses (or mass deficits instead) as well:

$$Q_{\alpha} = \left[m \binom{A}{Z} X_{N} - m \binom{A-4}{Z-2} Y_{N-2} - m(\alpha) \right] c^{2} = E_{D} + E_{\alpha}$$
 (2.23)

Applying the laws of energy and momentum conservation on the equation 2.23, the Q value can be calculated as

$$Q_{\alpha} = E_{\alpha} \frac{m(A-4 Y_{N-2}) + m(\alpha)}{m(A X_{N})} \approx E_{\alpha} \frac{A}{A-4}$$

$$(2.24)$$

and similarly, the kinetic energy of the daughter nucleus is

$$E_D = Q_\alpha - E_\alpha \approx E_\alpha \frac{A}{A - 4} - E_\alpha = E_\alpha \frac{4}{A - 4}$$
 (2.25)

For a nucleus with $Z \approx 200$, an α particle carries around 98% of the released energy and only around 2% is transformed into the recoil kinetic energy of the daughter nucleus.

The initial theory of α decay proposed that an α particle is formed within the nucleus prior to the decay [Gam28; Gur28]. This pre-formed α particle encounters a potential barrier that prevents its spontaneous emission from the nucleus. The height of this barrier can be determined using Coulomb's law, which is approximately 28 MeV for ²³⁸U, while the energy of the emitted α particles is around 4.2 MeV. According to classical mechanics, the emission of such α particles would be impossible. However, quantum mechanics allows for the possibility of an α particle to tunnel through the barrier with a certain probability. The emission of an α particle is the most favorable and efficient method of energy release due to its relatively high binding energy of ~28.3 MeV.

Because of the α -particle tunneling through the potential barrier, the half-life of the α decay is heavily dependent on the Q_{α} value. H. Geiger and J. M. Nuttall found a linear dependence between the logarithm of the decay constant and the range (and thus energy) of α particles [Gei11]. Later, this dependence became known as the Geiger-Nuttall law:

$$\log T_{1/2} = a(Z) + \frac{b(Z)}{\sqrt{Q_{\alpha}}} \tag{2.26}$$

The variables a(Z) and b(Z) vary for each isotopic series. There are several available theoretical approaches for partial α decay half-life determination, such as the model presented in [Poe80] with the set of updated parameters from [Poe06] or, alternatively, an approach described in [Qi09], which can be used also for the cluster emission half-life.

Another factor influencing the half-life of the α decay is the angular momentum change between the initial (I_i) and final (I_f) nucleus. The total spin of an α particle is zero, due to the arrangement of four constituent nucleons. The angular momentum carried away by the α particle after the decay is therefore purely of orbital character. Possible angular momentum values can be $|I_i - I_f| \leq L_{\alpha} \leq |I_i + I_f|$. The parity change is given by the selection rule given by the parity conservation: $\pi_i = (-1)^{L_{\alpha}} \pi_f$. Therefore, if the parity of the initial and final state are the same, L_{α} must be even and if the parities are opposite, L_{α} must be odd.

The α transitions between the same states (regarding angular momenta and parities) are strongly preferred. The more the states differ, the more the transitions between them are retarded. The hindrance factor (HF) evaluates the extent to which the experimentally measured transition is slower compared to an unhindered, theoretical prediction:

$$HF = \frac{T_{1/2, exp}}{T_{1/2, theor}}$$
 (2.27)

Another method to calculate the hindrance factor of an α decay is to compare reduced α decay widths of a certain transition δ^2 with unhindered (usually ground state (g.s.) \rightarrow ground state) transitions in neighbouring even-even nuclei δ^2_{e-e} :

$$HF = \frac{\delta_{e-e}^2}{\delta^2} \tag{2.28}$$

The reduced width of an α decay represents the decay stripped of the strong dependence on the decay energy. Reduced width is directly linked to the α decay probability as

$$\lambda_{\alpha} = \frac{\delta^2 P}{\hbar} \tag{2.29}$$

where P is the barrier penetration factor and defines the probability of an α particle penetrating the potential barrier. The penetration probability of an α particle carrying angular momentum L after an α decay with a Q value was derived by J. O. Rasmussen [Ras59]. The natural logarithm of the factor P is twice the Wentzel-

Kramers-Brillouin integral

$$\ln P = -2\frac{\sqrt{2m}}{\hbar} \int_{R_i}^{R_o} \left[V(r) + \frac{2Ze^2}{r} + \frac{\hbar L(L+1)}{2mr^2} - Q \right]^{\frac{1}{2}} dr$$
 (2.30)

where factor m is the reduced mass of an α particle and a daughter nucleus with atomic number Z, R_i and R_o are the inner and outer classical turning points. Simplified, R_i is the nuclear radius and R_o is the distance at which an α particle leaves the nucleus. The potential V(r) is defined as

$$V(r) = -1100 \exp\left(-\frac{r - 1.17A^{1/3}}{0.574}\right) \text{MeV}$$
 (2.31)

Based on the HF values, α transitions can be summarized as follows (according to [Lov06]):

- HF=1-4: favored transition. The populated states within mother and daughter nuclei are the same $(I_i^{\pi_i} = I_f^{\pi_f})$. Within odd A nuclei, favored transitions often lead to the excited daughter product, since the α particle is formed from a pair of nucleons from a lower-lying level.
- HF=4-10: transition between mixed or overlapping states.
- HF=10-100: transition with parallel initial and final spin projections, however, the wave function overlap is not favorable.
- HF=100-1000: transition between the states with parallel spin projections but with opposite parities.
- HF>1000: transition between the states with antiparallel spin projections and opposite parities.

2.3.2 Internal transitions

Nuclear decays and nuclear reactions often populate states energetically above the ground state in the final nucleus. These excited states are usually promptly deexcited to the ground or other excited states by internal transitions, that is either γ ray emission or internal conversion.

Emission of γ rays

The excited states of nuclei tend to promptly emit one or more photons to reach a more energetically favorable configuration. The energy range of the emitted photons can be from a few keV up to several MeV. In general, the energy balance of the emission of a photon with energy E_{γ} is

$$\Delta E = E_{\gamma} + T_N \tag{2.32}$$

where $\Delta E = E_i - E_f$ is the energy difference between the initial and the final state of the nucleus. The recoil energy of the nucleus T_N emerges from the conservation of linear momentum—the sum of the momenta of the nucleus and the emitted photon is zero $(\overrightarrow{p_N} + \overrightarrow{p_\gamma} = 0)$. The recoiling nucleus (with mass M) is non-relativistic, therefore the kinetic recoil energy can be expressed as

$$T_N = \frac{p_N^2}{2M} = \frac{p_N^2 c^2}{2Mc^2} = \frac{p_\gamma^2 c^2}{2Mc^2} = \frac{E_\gamma^2}{2Mc^2}$$
 (2.33)

For example, the recoil energy for 1 MeV photon emitted from the nucleus with $A{=}200$ is only ~ 3 eV, therefore in the cases of nuclear decay spectroscopy it is completely negligible since typical experimental resolutions of the detectors are in order of keV.

Discrete nuclear levels are described by their spin, parity, and excitation energy. The γ -ray emission is controlled by the conservation of energy and angular momentum and provides a large amount of information on the structure of nuclei. The angular momentum carried away by the γ ray with a quantum number L is determined by the momentum conservation as

$$|I_i - I_f| \le L \le |I_i + I_f| \tag{2.34}$$

where I_i and I_f are spin and quantum numbers of the initial and final levels, respectively. The multipole order of the transition is defined by the L quantum number: dipole for L=1, quadrupole for L=2, octupole for L=3, etc. Additionally, the parity of the γ ray depends on the angular momentum and the electric (E) or magnetic (M) character of the transition and is given as

$$\Delta \pi (EL) = (-1)^{L}$$

 $\Delta \pi (ML) = (-1)^{L+1}$ (2.35)

Consequently, the states with the same parity can be connected either by the even-L

electric of odd-L magnetic transition, while the deexcitation between opposite parity states can proceed by even-L magnetic or odd-L electric γ -ray emission. In general, EL and ML are called the multipolarity of the γ radiation and of the transition.

The lowest possible multipolarity of the transitions between $I_i=I_f$ states is a dipole transition with L=1. There are no monopole (L=0) transitions in which a single photon is emitted (classically, the monopole moment is the electric charge, which is static over time). For $I_i=I_f=0$ states the selection rules only allow a transition with L=0. In this case, the excited states decay through internal conversion, described in the following Sec. 2.3.2.

The rate (or the probability) of the transition heavily depends on its energy, character, and multipolarity and can be calculated using the following Wiesskopf single-particle estimates [Wei51]:

$$\lambda_{E}(L) \cong \frac{4.4(L+1)}{L[(2L+1)!!]^{2}} \left(\frac{3}{L+3}\right)^{2} \left(\frac{E_{\gamma}}{197 \,\text{MeV}}\right)^{2L+1} R^{2L} \times 10^{21} \,\text{s}^{-1}$$

$$\lambda_{M}(L) \cong \frac{1.9(L+1)}{L[(2L+1)!!]^{2}} \left(\frac{3}{L+3}\right)^{2} \left(\frac{E_{\gamma}}{197 \,\text{MeV}}\right)^{2L+1} R^{2L-2} \times 10^{21} \,\text{s}^{-1}$$
(2.36)

where the nuclear radius $R=1.25A^{\frac{1}{3}}$ is in $10^{-15}\,\mathrm{m}$ and E_{γ} is in MeV. These transition rates are shown graphically in Fig. 2.6 for $A{=}186$. In general, the magnetic transition is slower than its electric counterpart with the same multipolarity and this ratio between electric and magnetic transition decay constants is

$$\frac{\lambda_E}{\lambda_M} \approx 2.32R^2 \approx 2.9A^{\frac{2}{3}} \tag{2.37}$$

Generally, the experimental half-life of a state $T_{1/2}^{\gamma}$ differs from the partial half-life $T_{1/2}^{W}$ calculated by Eq. 2.36. For a mono-energetic decay, a correction for internal conversion is in the following form:

$$T_{1/2}^W = T_{1/2}^{\gamma} \times (1 + \alpha_{tot})$$
 (2.38)

where α_{tot} is the total conversion coefficient for all atomic shells, for more details see the next section. Similarly, other additional decay branches influence the partial half-life, increasing it correspondingly. Conventionally, the ratio between the experimentally measured and the calculated half-life represents the Weisskopf hindrance factor:

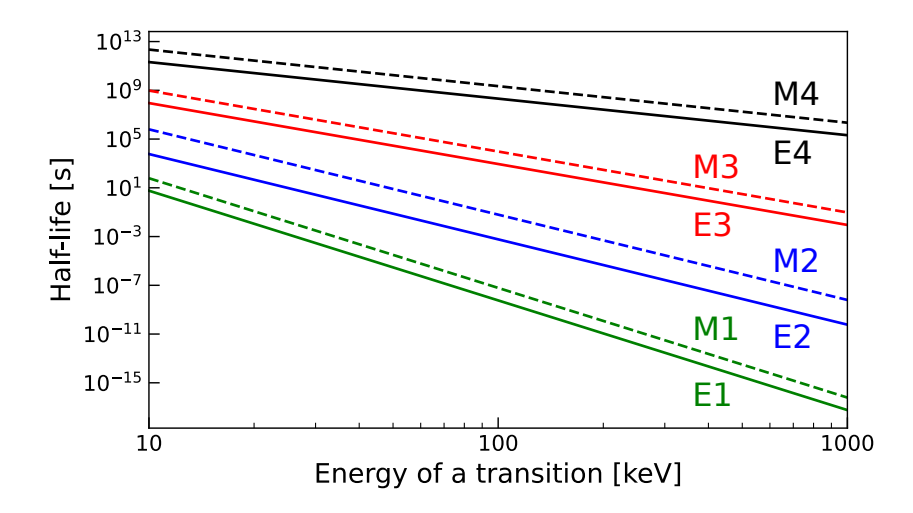


Figure 2.6: Wesskopf single-particle half-life estimates for A=186 calculated by Eq. 2.36 as a function of γ -ray energy.

$$F_W = \frac{T_{1/2}^{\gamma}}{T_{1/2}^W} \tag{2.39}$$

Albeit more complex nuclear models are necessary for a quantitative understanding of the physical changes inhibiting the isomeric transitions, the Weisskopf half-life estimates are accepted as useful benchmarks for comparison with experimental values. In general, the properties of the transition probabilities via γ -ray emission can be summarized as follows:

- The probability heavily depends on the energy of the transition. An increase of the energy by one order increases the probability by three orders and vice versa.
- Transitions with lower multipolarities are dominant. The probability of 100 keV transition of E1 is around five orders of magnitude higher than for E2 transition (for nuclei with $A \approx 200$).
- For a given energy and multipolarity, the electric transition probability is around two orders of magnitude higher than that of magnetic transition. Therefore, in the M2 transition, a small admixture of E1 can be present.

Internal conversion

Along the de-excitation via the γ ray emission, an excited nucleus can undergo a process called internal conversion (IC). The interaction between the electromagnetic

multipole fields of the nucleus and the atomic electron orbitals via the Coulomb force and the transferred energy can cause one of the electrons to be emitted. The energy of the emitted electron depends on the binding energy B_e needed to release the electron from the atomic orbital and the energy of the transition ΔE :

$$E_e = \Delta E - B_e \tag{2.40}$$

The binding energy of the electron in a particular shell therefore represents the threshold energy of the IC process. The conversion electrons (CE) are labeled according to the shell they were emitted from (K, L, M, ...), corresponding to the principal atomic quantum numbers n = 1, 2, 3...

After the emission of a conversion electron, the vacant place on the orbital is filled rapidly with an electron from the outer orbitals. The relocation of the electron from one shell to another causes the emission of X-rays which are characteristic for each element. The energy of the characteristic X-rays is given as the difference between the energies of the initial and final electron shells. Individual electron orbitals within the shell have slightly different binding energies. For example, the L shell (n = 2) consists of $2s_{1/2}$, $2p_{1/2}$, and $2p_{3/2}$ orbitals and the conversion electrons originating from these orbitals are referred to as L_1 , L_2 , and L_3 conversion electrons, respectively. Characteristic X-rays are therefore different for the electron relocations between $K - L_1$, $K - L_2$, and $K - L_3$ orbitals and are noted as K_{α_3} , K_{α_2} and K_{α_1} X-rays, respectively. A summary of the notations of the characteristic X-rays is in table 2.2 together with thallium X-ray energies and intensities as an example.

In the lead region, the X-ray intensities (and ratios between them) tend to not change significantly between the elements, therefore they are very similar to those of thallium from table 2.2. For 100 K-shell vacancies, K_{α_1} X-rays are the most intense with ~46% intensity, followed by K_{α_2} with ~27–28%, L_{α_1} with ~12–14%, K_{β_1} with ~11% etc.

The intensity of the emitted conversion electrons heavily depends on the multipolarity of the radiation. In some cases, the de-excitation of the excited states proceeds nearly exclusively via internal conversion, in others it is almost negligible compared with γ ray emission. In the transition probability calculations, both processes have to be considered. Therefore, the total decay probability of the excited state is

$$\lambda = \lambda_{\gamma} + \lambda_{IC} \tag{2.41}$$

Table 2.2: Notation for the characteristic X-ray transitions. Classical (Siegbahn) notation was first introduced in Ref. [Sie16]. Reference energies of X-ray transitions in thallium are from Ref. [Fir96]. The intensities are given per 100~K-shell vacancies.

Classical notation	Final – initial shell	X-ray energies in Tl [keV] (Intensity [%])
V	V I	72.87
K_{lpha_1}	$K-L_3$	(46.2)
K	K – L_2	70.83
K_{lpha_2}	$K - L_2$	(27.6)
K_{lpha_3}	K – L_1	70.18
n_{lpha_3}	$H = L_1$	(0.0395)
K_{eta_1}	K – M_3	82.57
n_{eta_1}	$K - M_3$	(10.7)
K_{eta_2}	$K - N_2 N_3$	84.87
n_{eta_2}		(3.9)
÷	:	i
L_{lpha_1}	$L_3 - M_5$	10.27
L_{lpha_1}	L_3 m_5	(12.4)
L_{lpha_2}	$L_3 - M_4$	10.17
L_{lpha_2}	$L_3 - W_4$	(1.39)
<u>:</u>	:	:

where λ_{γ} and λ_{IC} are the decay probabilities of γ ray emission and internal conversion, respectively. By defining the internal conversion coefficient (ICC)

$$\alpha = \frac{\lambda_{IC}}{\lambda_{\gamma}} \tag{2.42}$$

The total decay probability can be further expressed as

$$\lambda = \lambda_{\gamma} (1 + \alpha) \tag{2.43}$$

The decay probability of the IC is the sum of partial probabilities of the conversion on each shell $\lambda_{IC} = \lambda_{IC,K} + \lambda_{IC,L} + \lambda_{IC,M} + \dots$ and the total decay probability is then

$$\lambda = \lambda_{\gamma} + \lambda_{IC,K} + \lambda_{IC,L} + \lambda_{IC,M} + \dots = \lambda_{\gamma} (1 + \alpha_K + \alpha_L + \alpha_M + \dots)$$
 (2.44)

The following equations from [Kra88] give the estimate for the conversion coefficients of electric (E) and magnetic (M) multipole transitions in a nucleus with an atomic number Z:

$$\alpha(EL) \cong \frac{Z^3}{n^3} \left(\frac{L}{L+1}\right) \left(\frac{e^2}{4\pi\varepsilon_0 hc}\right)^4 \left(\frac{2m_e c^2}{E}\right)^{L+5/2}$$

$$\alpha(ML) \cong \frac{Z^3}{n^3} \left(\frac{e^2}{4\pi\varepsilon_0 hc}\right)^4 \left(\frac{2m_e c^2}{E}\right)^{L+3/2}$$
(2.45)

where n is the principal quantum number of the bound electron wave function and the term $e^2/(4\pi\varepsilon_0\hbar c)$ is the fine structure constant with a value of about 1/137. Theoretical values of conversion coefficients can be evaluated using a tool BRICC [Kib08].

The ICC of the transition can be determined from the number of experimentally measured γ rays N_{γ} and conversion electrons N_{CE} (corrected by the detection efficiency of the corresponding detector):

$$\alpha = \frac{N_{CE}}{N_{\gamma}} \tag{2.46}$$

The general properties of the internal conversion coefficients can be summarized as follows:

- The IC is significantly more probable in heavy nuclei than in the lighter ones due to \mathbb{Z}^3 dependence.
- The probability of the IC decreases with the increasing energy of the transition.
- The ICCs increase rapidly with the increasing transition multipolarity.
- For a given transition, the ratio between K and L conversion electron intensities is around 8, since the conversion on higher atomic shells decreases like $1/n^3$.

2.4 Nuclear isomerism

In addition to the lowest energy state—the ground state—a nucleus may also exist in a metastable excited state known as an isomer. The term isomer was adapted from chemical isomers whose constituents are the same but with different physical configurations. Analogically, nuclear isomers consist of the same particles arranged in different orbital configurations. Although there is no consensus on the definition of "metastable", it is typically considered an experimentally measurable time, with a lower limit of about a nanosecond $(10^{-9} \, \text{s})$. The half-life of isomers may reach up to 10^{16} years, as in the case of 180m Ta [Hul09], making 180m Ta the only naturally-occurring isomer.

A concept of nuclides having more than one configuration was proposed by Soddy in 1917 [Sod17]. The first experimental evidence of isomers was found in 234 Pa, where two β -decaying states were observed [Hah21]. Despite Soddy's proposal and Hahn's discovery, the concept of isomers faced considerable resistance. Only after Carl Friedrich von Weizsäcker provided a theoretical explanation in 1936 did the idea gain wider acceptance [Wei36].

The general concept of isomers is based on the existence of a secondary minimum in nuclear potential energy with respect to a variable parameter, such as spin, shape, or the projection of spin into the symmetry axis, as is shown in Fig. 2.7. In this situation, a transition to the energetically more favorable level requires a relatively large change of the parameter, hence hindering the transition significantly.

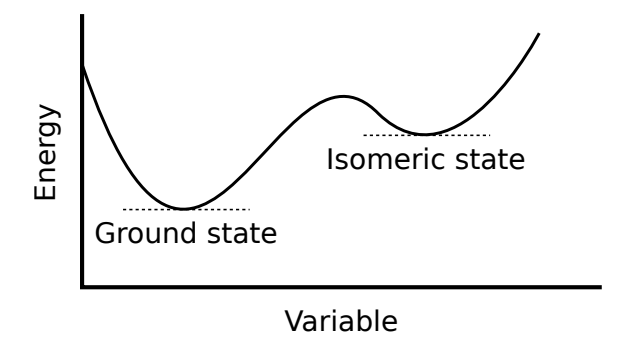


Figure 2.7: A schematic representation of an isomer as a secondary energy minimum of a function of a variable determining the type of isomer.

The occurrence of isomers is far from random, as can be seen from Fig. 2.8. The isomers cluster near the proton/neutron closed shells, especially at $Z \approx 50$, $N \approx 82$ and $Z \approx 82$, $N \approx 126$ where spherical nuclei are typical. Besides that, well-deformed nuclei in between the closed shells give rise to K isomers.

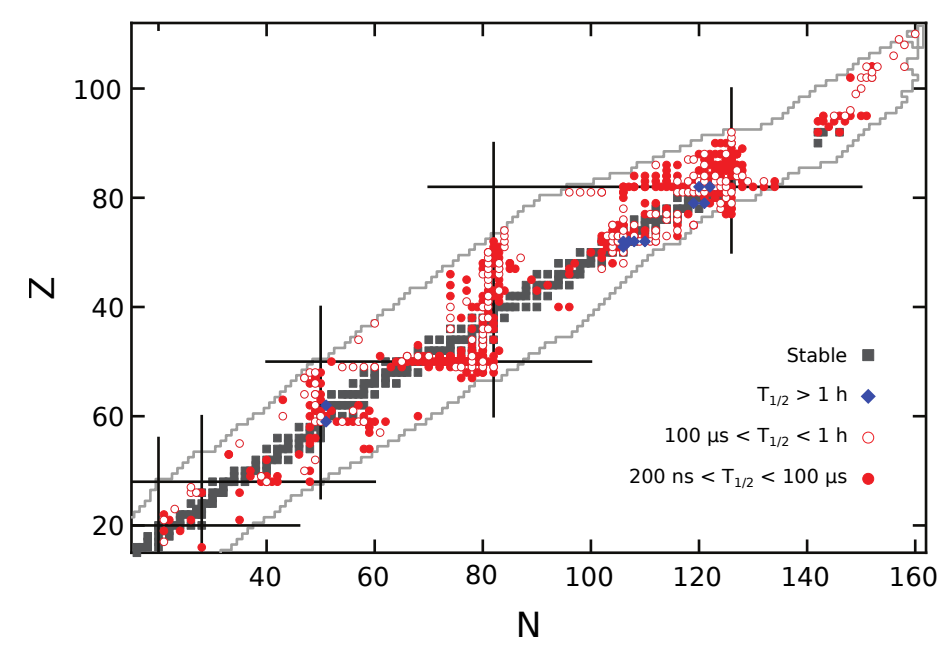


Figure 2.8: Nuclear chart showing the occurrence of isomers with excitation energies over 600 keV. Figure adapted and modified from Ref. [Dra16].

Spin isomers

Spin isomers were the first to be experimentally observed in 234 Pa [Hah21] and theoretically described [Wei36]. Spin isomers occur when a nucleus is trapped in an excited state with spin significantly different than lower-lying states, see 2.7. A deexcitation to these lower-lying states would require a large change of angular momentum, resulting in a high-multipolarity γ -ray emission. As was explained in Section 2.3.2, high-multipolarity transitions are highly hindered, therefore long-lived spin isomers are created. An extreme example of spin isomers is 180m Ta, where a large multipolarity of λ =7, 8 and low excitation energy results in its half-life of over 10^{16} years [Hul09].

A special type of spin isomers is seniority isomers. A quantum number seniority, ν , was introduced to explain atomic spectra [Rac43]. In nuclear physics, seniority denotes the number of nucleons that are not paired to an angular momentum of zero. Seniority is zero in the g.s. of even-even nuclei, where the lowest-energy excited states with ν =2 are created by breaking a nucleon pair. A typical examples of seniority isomers are found in semi-magic nuclei, for example, in the N=50 isotones 92 Mo, 94 Ru, 96 Pd, 98 Cd [Wal20]. Here, the two unpaired protons occupy the $g_{9/2}$ orbital and the resulting ν =2 states have spins of I=2, 4, 6, 8. The 8⁺ states become isomeric, due to a low-energy E2 transition between 8⁺ \rightarrow 6⁺ states.

K isomers

The existence of non-spherical nuclei led to their description in terms of deformed shapes and axis symmetry. Weizsäcker's explanation of isomerism revolved around the magnitude of angular momentum, whereas the nuclear symmetry axis implied that also the direction of angular momentum could be important. This realization led to the specification of the projection of the total angular momentum into the symmetry axis as a quantum number K and, consequently, K-forbidden transitions [Ala55]. Interestingly, the first cases of these so-called K isomers were observed prior to the theoretical description in 190 Os [Chu50] and 180 Hf [Bur51].

A transition of angular momentum λ is said to be K-forbidden, if the change ΔK of the K value is $\Delta K > \lambda$, with a degree of forbiddenness of $\Delta K - \lambda$ [Tan23]. K-forbidden transitions can be strongly hindered, even though they are not completely forbidden, due to K-mixing. An example is ¹⁷⁸Hf, where the 4-second K=8 isomer decays internally by an E1 transition with the Weisskopf hindrance of about 10^{13} [ENS24].

A typical locus of K isomers within the chart of nuclides is in-between the closed shells, at $Z \approx 75$, $N \approx 115$ ($A \approx 190$). Besides that, the region of superheavy elements at $Z \approx 100$, $N \approx 150$ ($A \approx 250$) is also known to contain K-isomers, such as K=8 isomers in 250 Fm and 254 No [Ghi73].

Shape isomers

The third type, known as shape isomers, is a consequence of a secondary minimum at large elongation of the nucleus. first discovered in ²⁴²Am [Pol62].

The decay of an isomer can proceed by the same means as of the ground states, i.e., by the α , β decay, fission, etc. In contrast to the ground state, the isomers can also decay internally, by either the γ -ray emission or the internal conversion, thus reaching lower excited states or the ground state.

Chapter 3

Experimental Background

In this chapter, a description of the Separator for Heavy Ion reaction Products (SHIP) and detection system will be presented. Electronic systems, signal processing, and correlation techniques will be explained as well.

3.1 Experimental production of nuclei

A beam of projectiles is provided by UNIversal Linear AC celerator (UNILAC), which can accelerate elements up to uranium (Z=92) to energies up to 20 AMeV (MeV per nucleon). Accuracy of the beam energy is ± 0.01 AMeV and beam intensities can reach 3 p μ A for ⁴⁰Ar⁸⁺, 1.2 p μ A for ⁵⁸Fe⁸⁺ and 0.4 p μ A for ⁸²Se¹²⁺ (1 p μ A (particle micro Ampere) = 6.24×10^{12} particles/s) [Hof00]. UNILAC operates in a pulse mode with 50 Hz frequency - one 20 ms macro-pulse consists of ~ 5 ms irradiation period (beam-on) and ~ 15 ms pause period (beam-off).

Accelerated beam is focused onto a target to the spot with a diameter of 5–10 mm [Fol95; Lom02]. The target consists of eight banana-shaped segments, each with dimensions of 110×23 mm, arranged into a circle with a diameter of 310 mm, see Fig. 3.1. The target material is evaporated onto a carbon foil about $35 \,\mu\text{g/cm}^2$ thin and covered with another $10 \,\mu\text{g/cm}^2$ carbon layer, to decrease sputtering and increase target emissivity. The targets are (0.1-1) mg/cm² thick, for lead and bismuth targets it is usually $\approx 500 \,\mu\text{g/cm}^2$. A thicker target leads to wider excitation functions (due to a larger distribution of energy losses of the projectiles in the target) which subsequently leads to the mixing of different evaporation channels and thus a higher background.

Projectiles can pass through inhomogeneities and pinholes in the target and



Figure 3.1: Eight-segment target wheel used at the experiments on SHIP.

increase background in the detector system. Therefore, a movable $(30-60) \,\mu\text{g/cm}^2$ carbon foil (also called charge-equilibration foil) is placed ~ 20 cm behind the target. The foil equilibrates the charge state of the reaction products and projectiles since the separator is optimized for particles with a particular charge state, while other states are suppressed.

The target wheel rotates synchronously with the beam macro-pulse structure to increase the irradiation area and thus avoid radiation damage and melting of the target [Mar79]. The rotation frequency is 18.75 Hz. Consequently, combined with the 50 Hz frequency of the beam-pulsing, the same target segment is exposed to radiation following a 160-millisecond cooling interval, equivalent to three complete rotations of the wheel. Furthermore, the low melting points of the commonly used materials, such as bismuth (271.4 °C) or lead (327.5 °C), can be compensated by using the compound targets with increased melting points—for example, PbS with 1130 °C and BiF₃ or Bi₂O₃ with 720 and 820 °C, respectively [Kin03; Kin06].

3.2 Nuclei separation - SHIP

Separator for Heavy Ion reaction Products (SHIP) located at GSI Darmstadt (Germany), is an electromagnetic separator, which uses kinematic properties of evaporation residues (ER) to separate them from other reaction products and projectiles based on their velocity [Mün79; Hof00]. Configuration of SHIP (Fig. 3.2) can be written as 3Q, E, 2M, 2M, E, 3Q, M, where Q is a magnetic quadrupole, E is an electric deflector and M is a dipole magnet. In principle, SHIP consists of two velocity filters (E, 2M) facing each other. In contrast to the classical Wien filter,

SHIP has separated electric and magnetic fields, which improves its efficiency and background suppression.

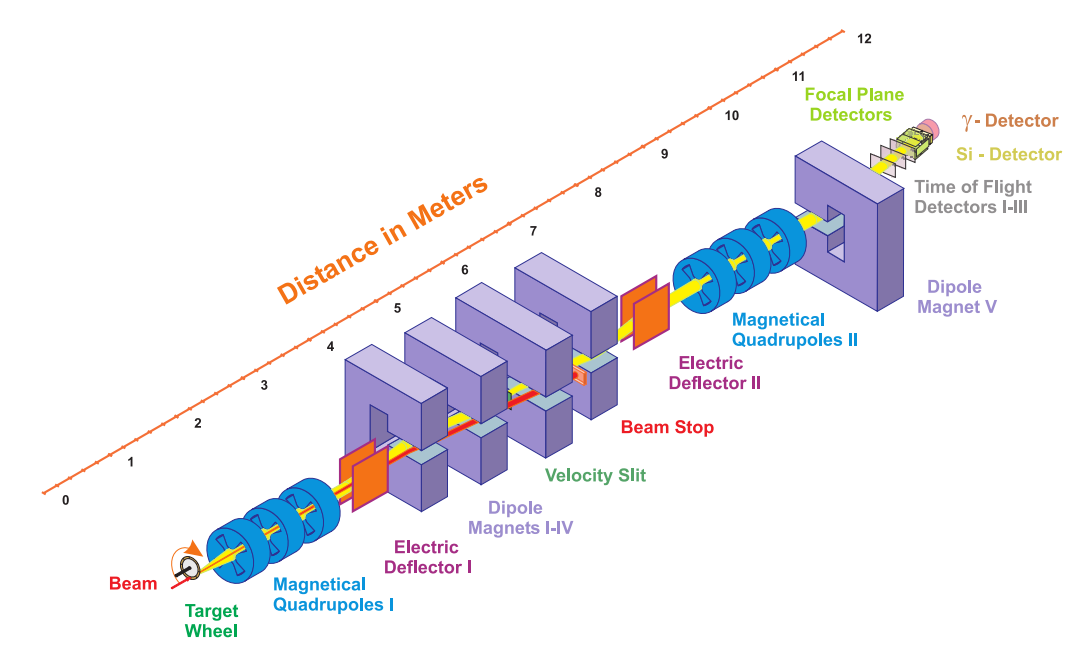


Figure 3.2: Velocity filter SHIP at GSI Darmstadt.

After the irradiation of the target, reaction products leave the target scattered at different angles. The focusation behind the target is done by the electro-magnetic lenses arranged as quadrupole triplet. Each magnet is turned by 120°, to ensure a uniform focusation. Afterwards, particles enter the ion-optical separator, where electric and magnetic fields perpendicular to each other interact on the charged particles by the Lorentz force:

$$F = qE + qvB$$

To pass the filter without deflection, Lorentz force has to be 0, therefore $qE = qvB \rightarrow E/B = v$. This allows for charged particles with a certain velocity to pass the filter independently on their charge. Since the target nuclei are at rest and therefore have zero momentum, the momentum of an ER is the same as that of a projectile. Due to higher mass, the velocity of ERs is lower than the velocity of projectiles, which allows setting a specific E/B ratio allowing only ERs to pass through the separator.

Another quadrupole triplet is placed behind the second electric deflector, to focus separated reaction products. One dipole magnet is further downstream to provide an additional 7.5° deflection to separate reaction products from high-energy

background passing through the separator.

SHIP accepts ions with a relative velocity width of $\pm 5\%$ and a charge state width of $\pm 10\%$. Flight time of the ERs through SHIP is around $2\mu s$. Total background suppression can reach the factor of $10^7 - 10^{11}$. The total transmission coefficient (ratio between the number of ERs entering the filter and the number of ERs leaving the filter) of the reaction products is heavily dependent on the mass (a)symmetry of the projectile and target nuclei. More symmetric reactions (e.g. 136 Xe+ 136 Xe) can reach up to 100% transmission, while very asymmetric reactions like 12 C+ 194 Pt reach only around 2%, see Fig. 3.3 and Ref. [Maz08]. After the separation, reaction products are implanted into the focal plane of the detector system.

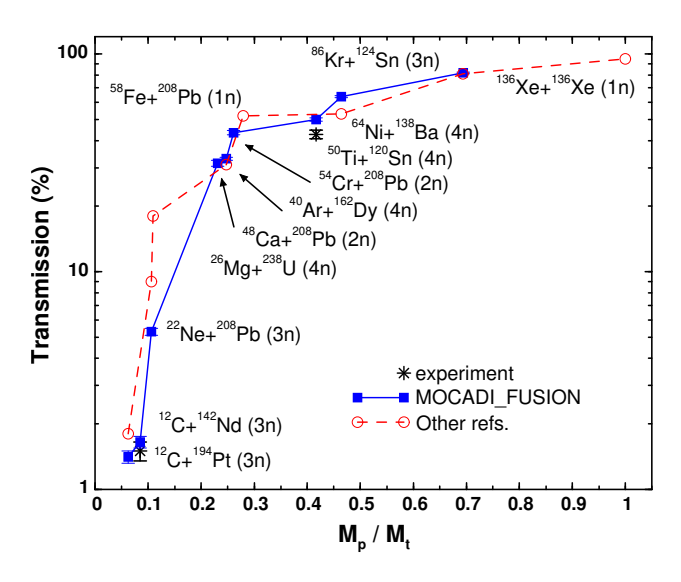


Figure 3.3: SHIP transmission - comparison of the experimental (black asterisks) and theoretical values calculated by the code MOCADI_FUSION (blue line). The red line represents values from [Pop97; Pop99]. Figure taken from [Maz08].

3.3 Detector system

After the separation, reaction products fly through the time-of-flight (TOF) system and are implanted into the detector system at the focal plane of the beam (Fig. 3.4).

The detector system consists of two or three TOF detectors, seven positionsensitive silicon strip detectors (PSSD) - one implantation PSSD (STOP) and six PSSDs in the backward direction (BOX), veto detector, and a germanium clover array.

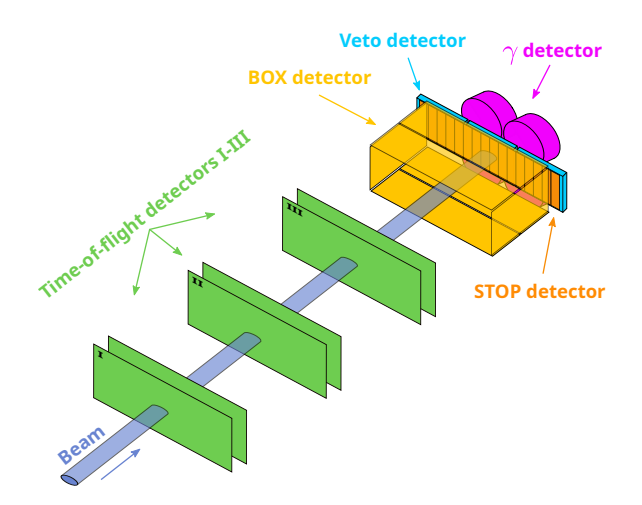


Figure 3.4: Detector setup behind SHIP (not to scale).

TOF system

Depending on the experiment, the TOF system consists of two or three TOF detectors 15 mm apart [Šár96]. Each TOF detector is made up of two self-supporting $30\,\mu\mathrm{g/cm^2}$ thick carbon foils, with $55\,\mathrm{mm^2}$ active area. After a reaction product passes a foil, electrons are emitted. An electric potential of 4 kV is applied between the foils to accelerate emitted electrons, while a perpendicular magnetic field bends electrons onto microchannel plates for amplification and signal reading. The transparency of the TOF system is 100% and the time resolution is 700 ps. The efficiency is around 99.8% for two and close to 100% for three TOF detectors. Anticoincidence between the TOF system and the STOP detector allows us to distinguish between signals induced by particles/nuclei coming from the separator and the signals induced by the decays of already implanted nuclei. From the time resolution of the TOF system and energy detected in the STOP detector, rough mass determination with an accuracy of $\pm 10\%$ is achievable [Hof00].

PSSD - STOP and BOX detectors

A PSSD consists of 16 silicon strips with a total active area of $35 \times 80 \,\mathrm{mm^2}$. Each strip is 35 mm long, 5 mm wide and $300 \,\mu\mathrm{m}$. Vertical position resolution is ~ $150 \,\mu\mathrm{m^1}$ for an α decay. Due to the position sensitivity, one PSSD is equivalent to 3700 single detectors, each with $0.15 \times 5 \,\mathrm{mm^2}$ active area. A typical energy resolution is $14 \,\mathrm{keV}$ for $^{241}\mathrm{Am}$ as an external source [Hof00]. All PSSDs are cooled down to $263 \,\mathrm{K}$.

¹All resolutions are noted as FWHM

In reality, a sum of an α -particle energy and the kinetic energy of the recoiling nucleus after an α decay is detected. Due to the pulse height defect affecting the detection of the recoiling nucleus, position resolution is worse - around 0.5 mm. The energy resolution is also affected by the pulse height defect, summing of the spectra from individual strips and non-ideal calibration and is around 20 keV,

One PSSD is placed in the focal plane of the beam coming from the separator. Here, ERs are implanted and stopped, hence the name STOP detector. Due to the range of α particles d_{α} (and fission fragments (FF)) in silicon being significantly larger than the range of ERs d_{ER} , α particles/FFs can escape the STOP detector in the backward direction without depositing full energy. This situation is displayed in Fig. 3.5.

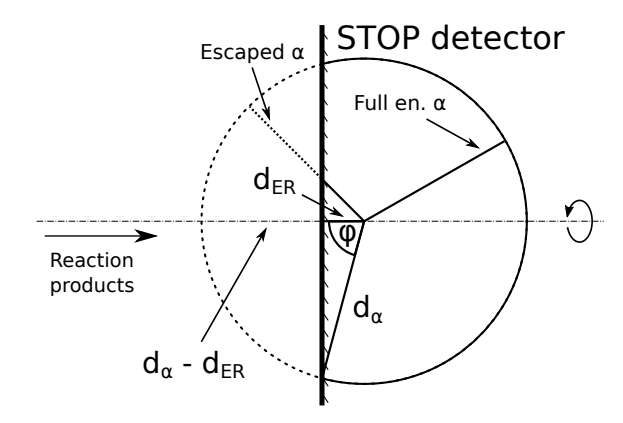


Figure 3.5: Geometric efficiency for detecting full-energy α particles after implantation into the STOP detector.

The ratio of α particles fully registered in the detector is calculated as the ratio between the areas of a sphere with the radius d_{α} and of a spherical cap of this sphere defined by the detector plane at a distance d_{ER} from the center of the sphere (solid curved line in Fig. 3.5). With the area of a spherical cap being $A_{cap} = 2\pi d_{\alpha}(d_{\alpha} + d_{ER})$, the geometric efficiency of the detector to fully register a particle is:

$$\varepsilon_{geom} = \frac{A_{cap}}{A_{sphere}} = \frac{2\pi d_{\alpha} (d_{\alpha} + d_{ER})}{4\pi d_{\alpha}^2} = \frac{1}{2} + \frac{d_{ER}}{2d_{\alpha}}$$
(3.1)

For example, in the 46 Ti+ 144 Sm reaction at 239.2-MeV beam energy, evaporation residue 186 Bi is implanted into the STOP detector with an energy of ~ 20 MeV (after energy lost in the target, TOF system, mylar degraders etc.) and decays via α decay with E_{α} = 7.2 MeV. The corresponding implantation depths are $d_{Re} \approx 3.6~\mu m$ and $d_{\alpha} \approx 41~\mu m$. From Eq. 3.1, the geometric efficiency of detecting full energy α particles is around 54.4%. Energy losses and implantation depths were calculated

with Lise++ software [Tar08].

To increase the geometric efficiency of the STOP detector, another six PSSDs are placed upstream of the beam in a box-like shape (hence the name BOX or BACK detectors). Neighboring strips of BOX detectors are connected galvanically, creating 28 segments. The geometric efficiency of the BOX detectors reaches 80% of 2π half-space in front of the STOP detector and the energy resolution of the STOP+BOX system is around 70 keV. This decrease in resolution (compared to ~ 20 keV of STOP detector) is because particles/FFs have to pass through dead layers of both STOP and BOX detectors, which is around $10 \,\mu\text{g/cm}^2$ thick. Coincidences between STOP and BOX detectors allow us to reconstruct the full energy of the α particles/FFs.

In front of the silicon detector array, degrader foils, usually from Mylar, can be installed. The thickness of foils can be adjusted in increments of $0.5\,\mu\mathrm{m}$ up to several $\mu\mathrm{m}$. Degrader foils are used to absorb low-energy projectiles passing through SHIP and to reduce the implantation depth of ERs (to eliminate low-energy "tails" from escaped particles). The ability to adjust implantation depth is crucial especially for the total kinetic energy determination of FFs, since the effect of the pulse-height defect varies with the implantation depth of ERs [Mos20].

Veto detector

A veto silicon detector is placed behind the STOP detector. Its purpose is to detect particles - usually high-energy protons - that pass through the STOP detector and are not registered by the TOF system. These signals are then rejected based on the coincidences between STOP-Veto detectors. Similarly to PSSDs, the Veto detector is cooled down to 263 K.

Germanium clover detector

Closely behind the array of silicon detectors, a germanium detector for the detection of X-rays and γ quanta is placed. In the past experiments, only one single germanium crystal was used, which did not allow measurement of the $\gamma - \gamma$ coincidences. Nowadays, a system of four identical germanium crystals arranged in a clover-like shape is used, hence the name clover detector. Two clovers with different volumes are usually used:

• VEGA type clover detector [Kas98]: four crystals with a diameter of 70 mm each and shaped and formed into a block with dimensions (124×124×140) mm³.

• The SHIP clover detector [Heß10]: four crystals with a diameter of (50-55) mm each and shaped and formed into a block with dimensions $(102 \times 102 \times 70)$ mm³.

VEGA clover provides better efficiency for detecting high-energy quanta, compared to the SHIP clover. The energy resolution of the germanium detectors is around (1.4-2.1) keV. Due to relatively low detection efficiency of around (10-12)% for 130 keV γ quanta, $\gamma - \gamma$ coincident measurements require relatively high statistics.

3.3.1 Calibrations

Ballistic, energetic (PSSD and Ge), position, efficiency, problems with the shift in R206 etc.

3.4 Methods for nuclear structure studies

3.4.1 Decay spectroscopy

alpha decay spectro, gamma spectro, beta decay spectro etc, problems, advantages, challenges

3.4.2 Other methods

Laser spectroscopy

e.g. ISOL methods, ISOLDE, short mention and description, nothing long, examples of facilities

In-beam spectroscopy?

same as in laser spectro, short description, examples of facilities

3.5 Data analysis

3.5.1 Electronics and signal processing

In an experiment, signals from different sources (particles, projectiles, transfer products, ERs, FFs, γ quanta, ...) with a wide variety of energies from a few keV to hundreds of MeV are registered, and processed.

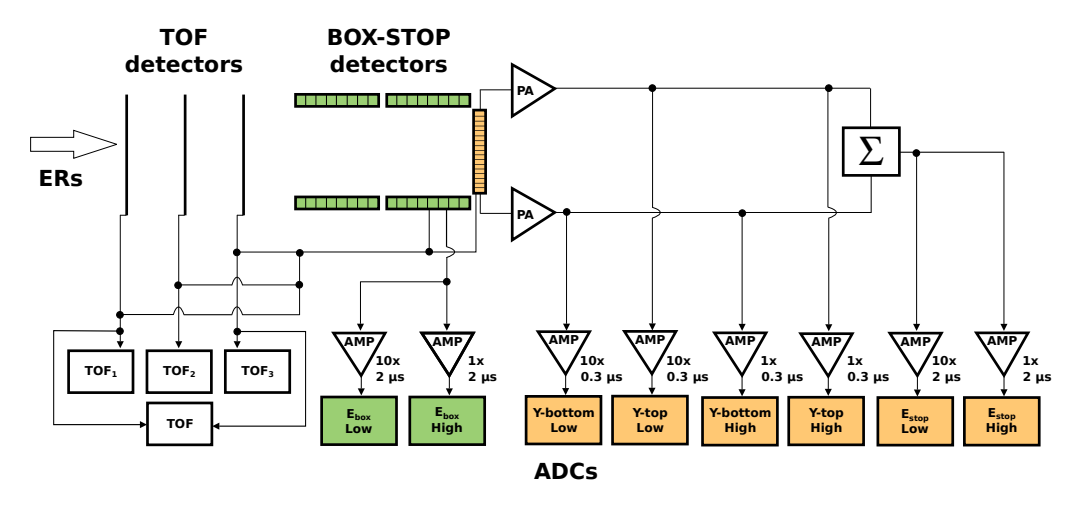


Figure 3.6: Schematic representation of the electronic system of STOP, BOX, and TOF detectors. Figure adapted from [Štr06].

The electronic system (Fig. 3.6) is divided into two branches, separate for lowand high-energy signals:

- Low-energy branch: processes signals up to ~ 16 MeV from the STOP and BOX detectors and up to ~ 1500 keV from germanium detectors with an amplification factor of 10.
- High-energy branch: processes signals from $\sim 4-300\,\mathrm{MeV}$ from the STOP and BOX detectors and up to $\sim 8\,\mathrm{MeV}$ from germanium detectors without an amplification.

Signals from the detector are processed with fast analog-to-digital converters with 3.5- μ s conversion time and 128-word first-in-first-out buffers in each channel [Hof00]. The signal width is determined by the shaping time constants—0.3 μ s is used for the position, and 2 μ s for the energy signals.

Time differences Δt (particle – γ) between particle- γ signals are handled based on the time intervals [Ant11]:

- Time differences Δt (particle γ) < 5 μ s are determined by the coincidence time of the data acquisition system and are measured with time-to-amplitude converters (TAC) with a resolution of 200 ns.
- Time differences Δt (particle γ) > 25 μ s are measured by a continuously running clock with a resolution of 1 μ s.

Time interval Δt (particle – γ)=(5–25) μ s is inaccessible due to the dead time of the data acquisition system.

In [Ant11], the time of the prompt coincidences was delayed by $\approx 0.8 \,\mu s$ and in the analysis TAC_{prompt}=0 μs was set. Therefore, coincidences of γ quanta emitted before the particles were measured as well (with TAC < 0 μs). Coincidences with TAC > 0 μs were due to γ quanta emitted after the particles within $\approx 2.6 \,\mu s$.

To determine the vertical position along the strip in the STOP detector, a signal is taken from the top and the bottom of the strip separately. The total energy is then the sum of the top and bottom signals. Position determination along the strip is done by comparing the energy signal from the top and bottom of the strip to the total energy. The BOX detector is not position-sensitive, due to the galvanic connections between the strips.

The analysis of experimental data is performed with the use of Object Oriented On-line Off-line system (Go4) [Ada08]. Go4 is based on the object-oriented analysis system ROOT [Bru97], with implemented extensions required for medium- and low-energy nuclear and atomic physics experiments.

3.5.2 Time-position correlation technique

This powerful technique was first introduced in 1979 and used in the α decay studies of the neutron deficient isotopes [Hof79]. It relies on the principle that the implantation and any subsequent α /SF decays of an ER and its daughter products have the same vertical position. The principle is shown in Fig. 3.7.

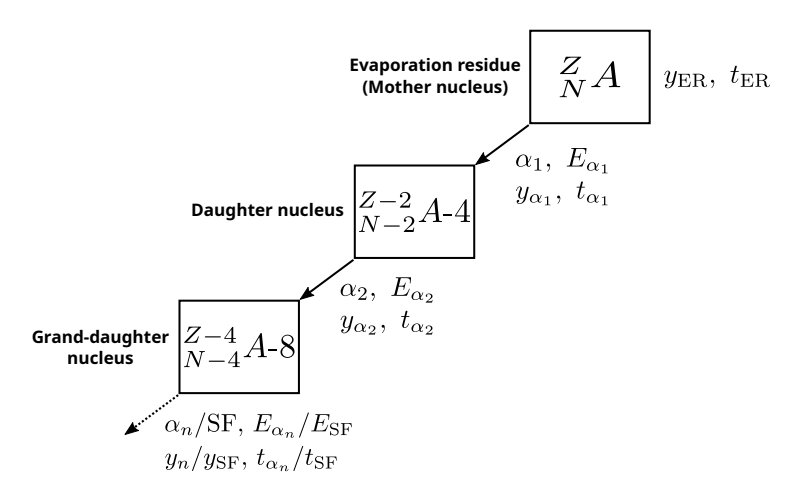


Figure 3.7: Correlation technique principle.

By adjusting correlation conditions, the technique enables us to study nuclei one by one and provides a significant background suppression, see the comparison in Fig. 3.8. Time window of around 3-5 times of the half-life of the corresponding nucleus

and position window of ~0.8 mm for α - α and ER- α were used throughout this work. The position window size was deduced from the correlation search of the short-lived isotopes (to reduce random correlations) and the corresponding position-difference distributions. The correlation technique enables the half-life determination of the studied nuclei and separation of the overlapping α -decay energies based on their different half-lives. New isotopes can be identified by reconstructing the decay chain from the decay of a known daughter nucleus back to the unknown mother nucleus. A special case is the correlation search of conversion electrons when the energy loss of electrons is not high enough to produce a position signal in the strip detector—therefore, in such cases, no position condition is used.

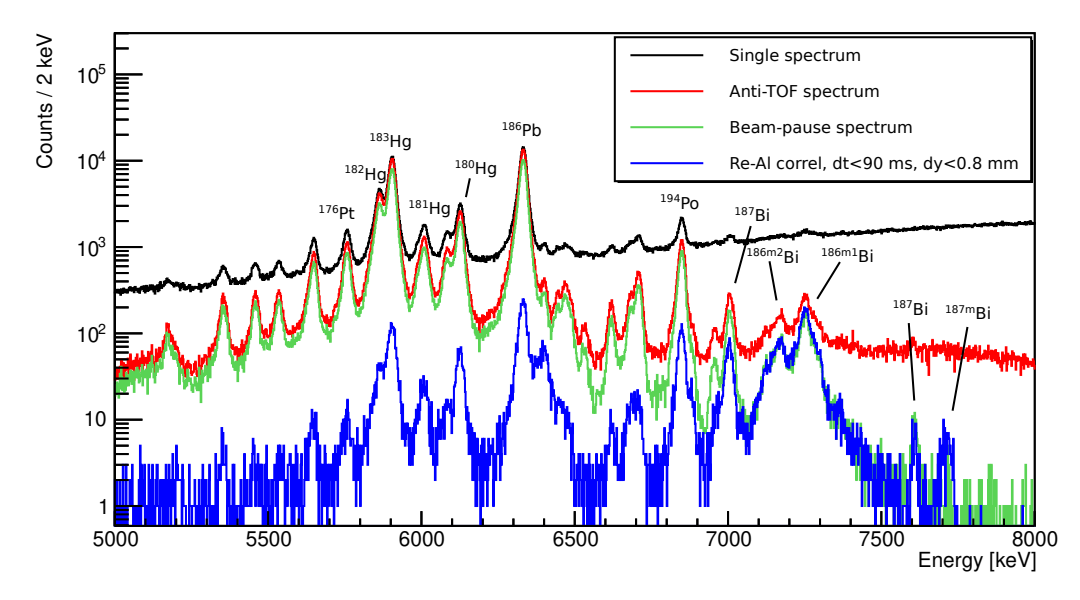


Figure 3.8: Effects of different methods for the background suppression. The black line represents all events in the STOP detector, the red line represents events in anti-coincidence with the TOF system, the green line shows events from the beam-pause and the blue line denotes events from the ER- α correlation search within 90 ms time window and 0.8 mm position window.

Fig. 3.8 demonstrates the effect of the correlation method. Nuclides ^{186,187}Bi have rather short half-lives with 10–15 ms of ^{186m1,m2}Bi, 0.37 ms of ^{187m}Bi and 37 ms of ^{187g}Bi. The correlation search with the time window of 90 ms does not reduce the number of decays of these isotopes in comparison to the beam-pause spectrum. On the other hand, the statistics of the longer-living isotopes with half-lives of 4.82 s (¹⁸⁶Pb), 0.392 s (¹⁹⁴Po) and 9.4 s ¹⁸³Hg are heavily reduced, by roughly two orders of magnitude, but are still present mainly as the random correlations.

3.5.3 Statistical analysis in case of poor statistics

The amount of the studied events is often not sufficient to use the statistical analysis. K.-H. Schmidt in [Sch84a] presented several relations to calculate the significance of correlated chains and estimate uncertainties of a number of events and half-lives, even in the case of singular events.

Random correlations evaluation

In case of high half-lives of the correlated nuclei, large time window conditions must be used and random correlations start to appear. The amount of random correlations n_r can be estimated as in [Sch84a]:

$$n_r = T\lambda_1 \dots \lambda_i \Delta t_{1,2} \dots \Delta t_{i,i+1} \tag{3.2}$$

where T is the total measure time, i is the total number of correlation groups, λ_i is the counting rate (events per second) of the corresponding group and $\Delta t_{i,i+1}$ is the corresponding correlation time window between i and i+1 group. The counting rate also reflects the correlation position window.

Error determination for small numbers

Countrate uncertainties - Poisson distribution The probability of observing n events while μ is the mean value of the number of events is described by the Poisson distribution:

$$p(n \mid \mu) = \frac{\mu^n}{n!} e^{-\mu} \tag{3.3}$$

For the confidence level $(1 - \varepsilon)$ (ε is an error probability) and observed events n_m , the confidence lower (μ_l) and upper (μ_u) limits are given as the solutions of the following equations:

$$\sum_{n=n_m}^{\infty} p(n \mid \mu_l) = 1 - \sum_{n=0}^{n_m-1} \frac{\mu_l^n}{n!} e^{-\mu_l} = \frac{\varepsilon}{2}$$

$$\sum_{n=0}^{n_m} p(n \mid \mu_u) = \sum_{n=0}^{n_m} \frac{\mu_u^n}{n!} e^{-\mu_u} = \frac{\varepsilon}{2}$$
(3.4)

An accurate approximation of the lower and upper confidence limits for small numbers and $n_m \ge 2$ is

$$\mu_l \approx n_m - z\sqrt{n_m}$$

$$\mu_u \approx n_m + z(1 + \sqrt{n_m})$$
(3.5)

Parameter z is related to the chosen confidence level $(1-\varepsilon)$ through

$$\frac{\varepsilon}{2} = \int_{z}^{\infty} \frac{1}{\sqrt{2\pi}} e^{-x^{2}/2} dx \tag{3.6}$$

and for the standard error z = 1 (confidence level $(1-\varepsilon) = 0.68$). This approximation for small numbers is much more accurate than the conventionally used symmetric errors

$$n_m - \mu_l = \mu_u - n_m = z\sqrt{n_m} \tag{3.7}$$

Comparison of the exact confidence limits given by the equation 3.4, the approximation by the equation 3.5 and the symmetric errors (Eq. 3.7) is in Fig. 3.9a. Standard errors for $n_m \leq 2$ are summarized in Tab. 3.1.

Lifetime uncertainties - exponential distribution The arithmetic mean $\overline{t_m}$ of the lifetimes $(t_m)_i$ at which the events were observed gives the maximum likelihood estimate of the lifetime τ :

$$\overline{t_m} = \frac{1}{n} \sum_{i=1}^{n} (t_m)_i \tag{3.8}$$

The confidence lower (τ_l) and upper (τ_u) limits of the lifetime determination of n observed events can be expressed as the solution of the following equations

$$\int_0^{\overline{t_m}} p_n(t|\tau_u) d\overline{t} = 1 - \sum_{n=0}^{n-1} \left(\frac{n\overline{t_m}}{\tau_u}\right)^n \frac{1}{n!} e^{-n\overline{t_m}/\tau_u} = \frac{\varepsilon}{2} (3.9)$$

where $\overline{t_m}$ is the observed value for \overline{t} and \overline{t} is the mean observed value. An accurate approximation for these confidence limits for small numbers and $n \ge 2$ is

$$\tau_{l} \approx \frac{\overline{t_{m}}}{1 + z/\sqrt{n}}$$

$$\tau_{u} \approx \frac{\overline{t_{m}}}{1 - z/\sqrt{n}}$$
(3.10)

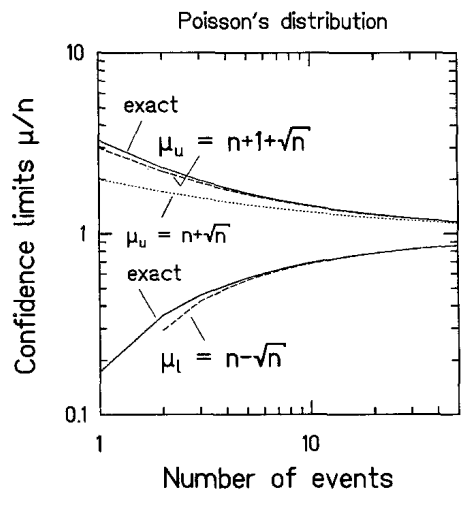
Parameter z is expressed by the equation 3.6. This approximation is much more accurate than the conventionally used symmetric errors

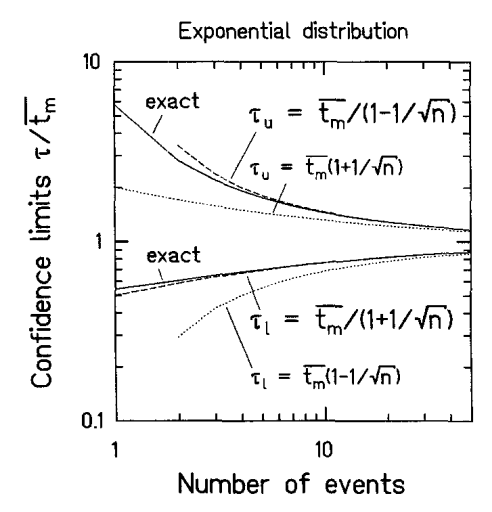
$$\overline{t_m} - \tau_l = \tau_u - \overline{t_m} = z \frac{\overline{t_m}}{\sqrt{n}} \tag{3.11}$$

Comparison of the exact confidence limits given by the equation 3.5.3, the approximation by the equation 3.10 and the symmetric errors (Eq. 3.11) is in Fig. 3.9b. Standard errors (confidence level $(1 - \varepsilon) = 0.68$) for $n_m \le 2$ are summarized in Tab. 3.1.

Table 3.1: Standard errors (confidence level $(1-\varepsilon) = 0.68$) for number of observed events $n \le 2$, calculated from the equations 3.4 (Countrate column) and 3.5.3 (Lifetime column). Cases where the approximations by the equations 3.5 and 3.10 are within 10% from the exact values are given in parentheses.

Number of observed counts n	Countrate		Lifetime	
	μ_l	μ_u	$\tau_l/\overline{t_m}$	$\tau_u/\overline{t_m}$
0	0	1.84	-	-
1	0.173	(3.3)	(0.543)	5.79
2	(0.708)	(4.64)	(0.606)	(2.82)





- (a) The confidence limits of the events following the Poisson distribution.
- (b) The confidence limits of the events following the exponential distribution.

Figure 3.9: Confidence limits for a confidence level $(1-\varepsilon) = 0.68$ (z=1) as the functions of observed events. Solid lines denote exact values derived from the equations 3.4 and 3.5.3, dashed lines are approximations from the equations 3.5 and 3.10, in figs. 3.9a and 3.9b, respectively. Dotted lines denote conventional symmetric errors. Figure reprinted from [Sch84a].

Chapter 4

Results and discussion

In this chapter, we present and discuss the results from two independent analyses. The first part focuses on the study of production systematics of fusion-evaporation reactions leading to compound nuclei around radon (Z=86). The results from the analysis of experimental data from three fusion-evaporation reactions leading to 199,201,202 Rn* measured at SHIP are presented and discussed. Additional cross section data for the reactions leading to radon and astatine compound nuclei were extracted from the literature. From the comparison of experimental and theoretical excitation functions by the statistical model code HIVAP, a fission-barrier scaling parameter was determined for each reaction, and a function of the barrier-scaling with respect to the mass number of the compound nucleus was derived for radon and astatine isotopes.

The second part revolves around the decay spectroscopy of 186 Bi based on data measured at two experiments at SHIP. The new results derived from the α - γ coincidence analysis are presented and an updated decay scheme of both isomers in 186 Bi is proposed. An extensive discussion of the situation in even-A light bismuth isotopes, regarding the level configurations, recent results and is presented as well. The main results from this analysis will be submitted in the journal Physical Review C—draft of the article is ready ADD A REFERENCE (TO BE SUBMITTED).

Table 4.1: The α -decay properties of radon isotopes produced in the reactions $^{52}\mathrm{Cr}+^{147,149,150}\mathrm{Sm} \rightarrow ^{199,201,202}\mathrm{Rn}^*$ at SHIP separator.

Mother	Daughter	$E_{lpha} \; [ext{keV}]$	$T_{1/2} \; [\mathrm{ms}]$	b_{lpha}	Ref.
$^{195}\mathrm{Rn}$		7536	6	1	[Ket01]
	$^{191}{\rm Po}$	~7335	22	0.909	[And02]
$^{195m}\mathrm{Rn}$		7555	5	1	[Ket 01]
	$^{191m}\mathrm{Po}$	7376	93	0.457	[And02]
$^{196}\mathrm{Rn}$		7462	4.4	0.998	[ENS24]
	192 Po	7167	32.2	0.986	[ENS24]
$^{197}\mathrm{Rn}$		7260	55	1	[Enq96; And08]
	193 Po	6948	388	0.993	[ENS24; Van02]
$^{197m}\mathrm{Rn}$		7356	24	1	[And08]
	$^{193m}\mathrm{Po}$	7002	245	0.992	[ENS24; Van02]
¹⁹⁸ Rn		7196	65	0.99	[ENS24]
	194 Po	6843	392	0.927	[ENS24]
¹⁹⁹ Rn		6989	590	0.94	[ENS24; Tay99; Uus05]
	195 Po	6611	4640	0.936	[ENS24]
$^{199m}\mathrm{Rn}$		7060	310	0.97	[ENS24; Tay99; Uus05]
	$^{195m}\mathrm{Po}$	6700	1920	0.9	[ENS24]
²⁰⁰ Rn		6902	960	0.98	[Cal84; Wau93]
	¹⁹⁶ Po	6522	5600	0.94	[ENS24]

4.1 Production of isotopes from radon region

4.1.1 Reactions leading to radon compound nuclei

The experimental data from three fusion-evaporation reactions $^{52}\text{Cr}+^{147,149,150}\text{Sm}\rightarrow^{199,201,202}\text{Rn}^*$ were analysed. All three reactions were measured at SHIP separator, in GSI, Darmstadt. The experimental details are summarized in Table 4.2. In all three reactions, the beam of ^{52}Cr projectiles with varying energies was used, allowing a precise measurement of the corresponding excitation functions.

Beam intensity Target thickness Beam energy CNBeam **Target** $[\mu \mathrm{g/cm^2}]$ [MeV][pnA] $^{147}\mathrm{SmF}_{3}$ 199Rn* 540 - 670222 - 261496 $52 Cr^{13+}$ $^{149}\mathrm{SmF}_{3}$ $^{201}\mathrm{Rn}^{*}$ 670 - 930219 - 251464 $^{150}\mathrm{SmF}_3$ $^{202}Rn^*$ 790 220 - 236338

Table 4.2: Experimental details of the reactions leading to radon compound nuclei measured at SHIP separator.

The short half-lives of both mother and daughter isotopes produced in the studied reactions allowed the use of Recoil- α - α correlation search, for more details see Section 3.5.2. In all cases, a correction for the real number of events was used to compensate for the loss of statistics due to half-lives $T_{1/2}$ and correlation time windows ΔT :

$$N_{real} = N_{det} \times \left(1 - e^{-\ln 2\frac{\Delta T}{T_{1/2}}}\right) \tag{4.1}$$

This correction is especially significant in the case of heavier evaporation residues produced in the analyzed reactions, such as 199,200 Rn, where the correlation time windows were comparable or shorter than the half-lives. The SHIP transmission of 50(10)% for the 52 Cr- 147,149,150 Sm projectile-target combination was used in the analyzed reactions, see Sec. 3.2 and Fig. 3.3. The stated uncertainties in Table 4.2 are statistical only; the absolute uncertainties regarding primarily the uncertainty of the transmission efficiency of SHIP are estimated to be $\pm 25\%$.

Reaction ⁵²Cr+¹⁴⁷Sm→¹⁹⁹Rn*

The reaction leading to the lightest studied radon compound nucleus, 199 Rn*, was measured at four beam energies above and two below the fusion barrier. The 2–4n evaporation channels were observed, corresponding to the $^{197-195}$ Rn ERs, respectively. These produced radon isotopes have well-defined α -decay energies as well as relatively short half-lives, see Tab. 4.1, allowing the use of the ER- α - α correlation search with narrow time windows ADD AN EXAMPLE 2D E_M – E_D CORRELATION MATRIX?. The evaluated cross sections are summarized in Table 4.3 and the resulting excitation functions, together with the HIVAP calculations, are displayed in Fig. 4.1.

^{*} Beam energy in the middle of the target

[†] The thickness of the compound target

Interestingly, the isotope ¹⁹⁵Rn was also produced at much higher energy than the calculations predicted. An explanation is that the element samarium has seven naturally abundant isotopes—¹⁴⁴Sm, ^{147–150}Sm, ¹⁵²Sm, and ¹⁵⁴Sm. The isotopic enrichment of the targets does not eliminate undesired isotopes of the target material entirely, which are therefore present in the enriched targets as admixtures FIND AND ADD CITATION. Especially heavier isotopes of the target material may influence the production of isotopes significantly.

Besides the admixtures, the non-zero thickness of the targets leads to the spread of the projectile energies due to the energy losses within the target material. As a result, the experimental excitation functions are wider than the theoretical ones, which is seen in the case of, for example, ¹⁹⁶Rn. Combining the isotopic admixtures and the wider projectile energy intervals results in experimental excitation functions with shapes that are not perfectly reproduced by the theoretical HIVAP calculations. However, the maxima of the experimental and theoretical excitation functions are not affected by the mentioned effects and therefore present a good benchmark for the determination of an ideal fission barrier-scaling parameter of the HIVAP calculations.

The best reproduction of the experimental data from the $^{52}\text{Cr}+^{147}\text{Sm}\rightarrow^{199}\text{Rn}^*$ reaction was achieved by the HIVAP with the barrier-scaling parameter of 0.62, deduced mainly from the maxima of 3n (^{196}Rn) and 4n (^{195}Rn) evaporation channels near/above the fusion barrier. The maximum of the 2n channel (^{197}Rn) lies below the fusion barrier, where the reliability of the HIVAP is rather uncertain, however, in this case, this excitation function is well reproduced as well.

Reaction 52 Cr + 149 Sm $\rightarrow ^{201}$ Rn*

The second reaction $^{52}\text{Cr} + ^{149}\text{Sm} \rightarrow ^{201}\text{Rn}^*$ was measured at seven beam energies, three of them above the fusion barrier. Four evaporation channels were observed, 2-5n, corresponding to the ERs of $^{199-196}\text{Rn}$, respectively.

Reaction
$${}^{52}\mathbf{Cr} + {}^{150}\mathbf{Sm} \rightarrow {}^{202}\mathbf{Rn}^*$$

asdf

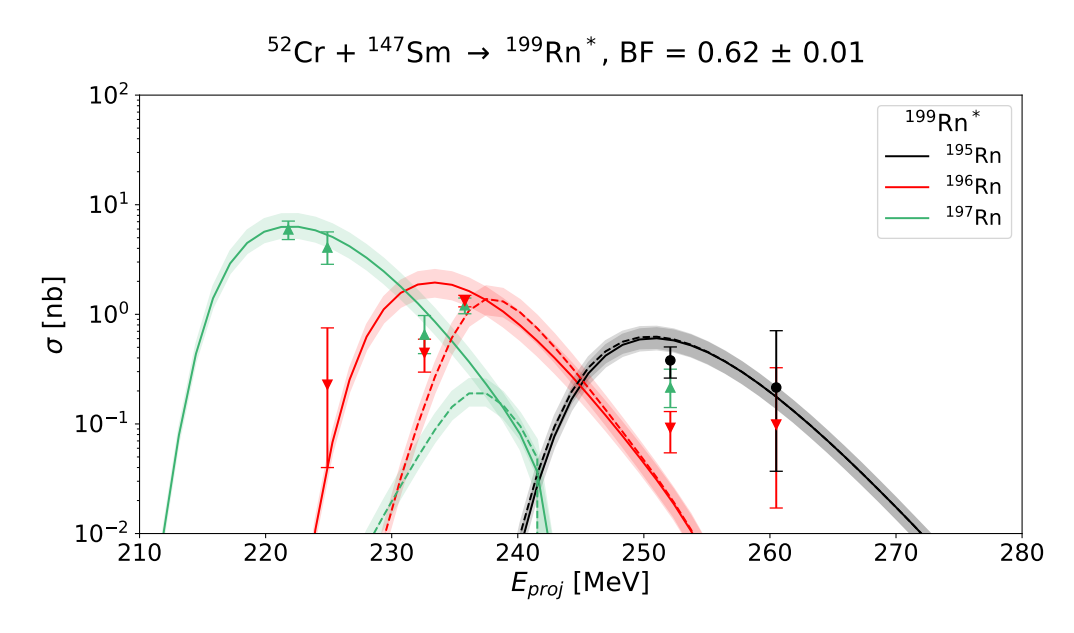


Figure 4.1: The experimental (points) and theoretical (lines) excitation functions for the reaction $^{52}\text{Cr}+^{147}\text{Sm}\rightarrow^{199}\text{Rn}^*$. The solid lines denote the HIVAP calculations according to the BF approach, the dashed lines are for the IP parametrization, see Sec. 2.1.1. The matching semi-transparent shadow around the lines denotes the calculation with the BF±0.01 parameter.

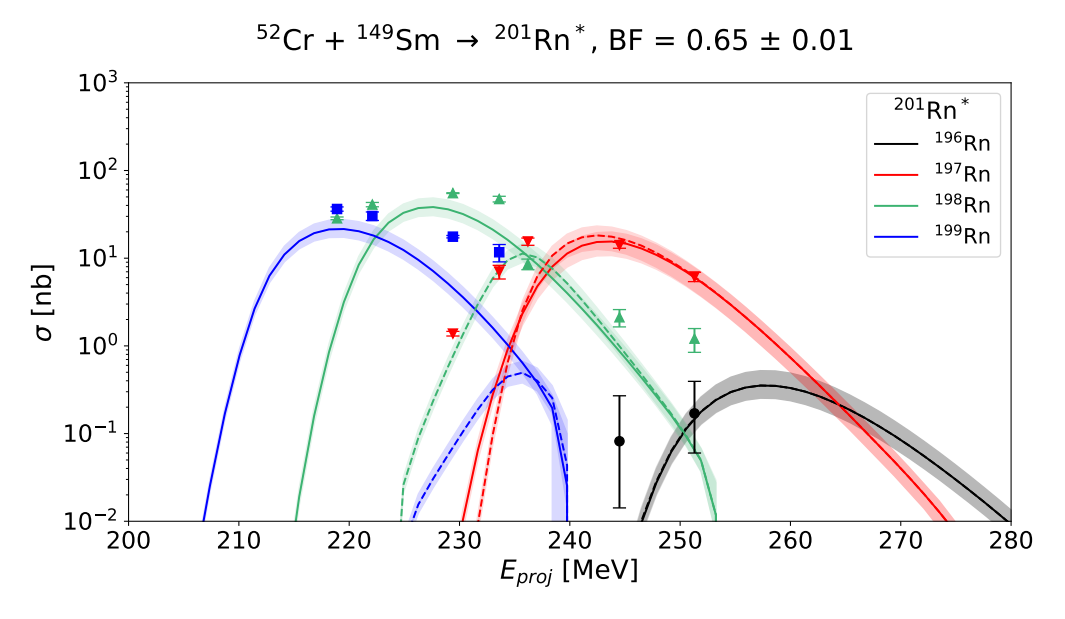


Figure 4.2: The same as in Fig. 4.1, but for the reaction ${}^{52}\text{Cr} + {}^{149}\text{Sm} \rightarrow {}^{201}\text{Rn}^*$.

Summary of analyzed data

Literature data

4.1.2 Reactions leading to a tatine compound nuclei

Reaction to 192,193 At*

Literature data

51

4.1.3 Barrier-scaling systematics

• Description of experiments at SHIP where Rn* data were collected, with table

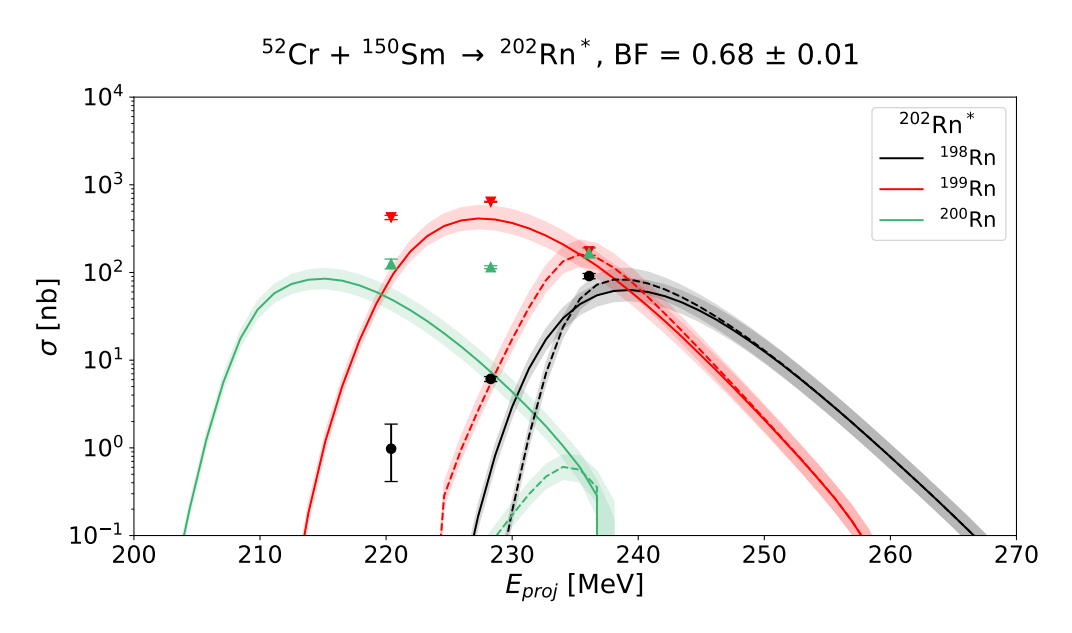


Figure 4.3: The same as in Fig. 4.1, but for the reaction ${}^{52}\text{Cr} + {}^{150}\text{Sm} \rightarrow {}^{202}\text{Rn}^*$.

- Specification of methods used (Re-Al-Al correlations) and their conditions, some challenges (such as close alpha decay energies/half-lives), uncertainties (statistical, SHIP's transmission...), what is the biggest contributor to uncertainty/background etc.
- Afterwards, show the results from SHIP reactions, for each reaction separately, show Re-Al-Al spectra (matrices). Then, show excitation functions with HIVAP calculations and a short discussion, about e.g. problems, accuracy etc. Summarize cross sections in a table. In the table, show also half-lives and α decay energies of the determined ERs, so it will be easier to refer to it (then, maybe put the table earlier in the section, so it is more "accessible"?).
- Description of data from AGFA (192, 193At*), what were the challenges, expectations etc. cite the proposal and the PRC paper. Maybe mention here also Hao's 182,183Bi paper?
- Then proceed with literature data description of data from the literature for Rn* and At*, where they were measured, what is the "reliability" of data etc.
- HIVAP calculations: the figs with cross section data and corresponding HIVAPs
 will probably go into APPENDIX, since there are lots of them. Discuss the
 reliability of HIVAPs here, especially for literature data (analysed radons discussed separately), how were the BARFACs determined, what is the uncer-

tainty, how well they reproduce exp. data etc.

- Afterwards, shortly discuss fission-barriers (compare different models), mention that the scaling is well-known from other experiments (for example, Andrei's cross section paper, or Veselsky's recent one https://doi.org/10.1103/PhysRevC.109.014618).
- Proceed to the deduced scaling systematics, how it compares to Bi/Po Andrei's one. Discuss potential effects of quasi fission on the lightest isotopes, show the QF systematics from du Rietz' paper (ofc, for reactions studied here), maybe link to Bi CNs and Hao's "unobservation" of 182,183Bi.
- If done, compare 210Rn* data from SHIP and deduced BF to Veselsky's values.
- An outlook about the future of production of very neutron-deficient isotopes, (a)symmetric reactions, quasi fission hindering, experimental challenges, new/more precise/reliable models for cross section calculations (NRV, coupled channels etc.) [description, if barrier-scaling can be a factor there as well, complexity, easy-to-use etc.] in comparison to HIVAP an example could be shown between some reaction. I'll probably move this to Conclusion and Outlook at the end.

4.2 Decay spectroscopy of ¹⁸⁶Bi

4.2.1 Experimental details

Describe both experiments, give details in the table (probably the same as in paper), what were some problems (e.g. differences between PSSD calibrations, how they were resolved, Ge calib. in Exp1 etc). Maybe this should be summarized in the previous chapter? Then, I should move also exp. details for cross-section stuff to exp. section?

4.2.2 Results and discussion

In results show spectra, the same as in paper - Re-Al, discuss why there is difference between 7150 and 7250-keV peak ratios (no conclusion), summarize half-life analysis, maybe show decay curves, discuss different results between experiments. Show Al-Ga matrix, maybe summarize Ga peaks in a table with corresponding Al energies.

Discuss background between the Ga lines, maybe show all projections gated by gammas. Discuss certain Al-Ga transitions (108, 445, 520, maybe 371, 426 keV) and place them into the decay scheme. Discuss other possible candidates, what are the problems there (strange, wide, uncertain Al distributions). Suggest the placement of these "strange" gamma transitions into the decay scheme, consider Al+CE summing and Geant4 simulations (mention/compare it to Andrei's verification of E1 character of 108 keV transition in 186Bi).

Outlook - consider other possibilities to study 186Bi, maybe via 190At decay (and link it to the cross section studies), in ISOLDE (maybe some limitations etc.), other possible means of production (maybe find some other reaction?). Mention some improvements what could be done, more Ge detectors, higher stats, etc.

Table 4.3: The cross section values for the three analyzed reactions measured at SHIP by the evaporation channel. Asymmetric uncertainties are reported for data points with low statistics and were calculated as described in Sec. 3.5.3. The data with the theoretical calculations by the HIVAP code are also presented in Figs. 4.1, 4.2 and 4.3

		$\sigma [{ m nb}]$			
Reaction	$E_{proj} \left[\mathrm{MeV} ight]^*$	2n	3n	4n	5n
	221.8	6.0(11)			
	224.9	$4.1^{+1.6}_{-1.2}$	$0.2^{+0.5}_{-0.2}$		
$^{52}\mathrm{Cr} + ^{147}\mathrm{Sm} \rightarrow ^{199}\mathrm{Rn}^*$	232.6	$0.7^{+0.3}_{-0.2}$	0.5(2)		
(Fig. 4.1)	235.8	1.2(2)	1.3(2)		
	252.1	0.2(1)	0.09(4)	0.4(1)	
	260.5		$0.1^{+0.2}_{-0.1}$	$0.2^{+0.5}_{-0.2}$	
	218.9	36(2)	28(1)		
	222.1	30(3)	41(2)		
⁵² Cr+ ¹⁴⁹ Sm→ ²⁰¹ Rn*	229.4	18(1)	55(1)	1.4(1)	
	233.6	12(3)	47(4)	7.0(12)	
(Fig. 4.2)	236.2		8.6(12)	16(2)	
	244.5		2.1(5)	14(1)	$0.08^{+0.19}_{-0.07}$
	251.3		1.2(4)	6.2(8)	$0.2^{+0.2}_{-0.1}$
$52 \text{Cr} + 150 \text{Sm} \rightarrow 202 \text{Rn}^*$	220.4	130(16)	430(24)	$1.0^{+0.9}_{-0.6}$	
	228.3	120(4)	640(8)	6.1(4)	
(Fig. 4.3)	236.1	170(22)	170(17)	91(6)	

 $^{^{\}ast}$ Beam energy in the center of the target. Energy losses were calculated with the Lise++ software [Tar08]

Table 4.4: Reactions used in this work to deduce the barrier-scaling parameter. The uncertain BF values are denoted by italics. Reaction denoted by * was recently measured at the Argonne National Laboratory and the data are not published yet. The results from the reactions denoted by † symbol are from unpublished data from SHIP separator analyzed in this work, see Sec. 4.1.1 and 4.1.2. The presented barrier-scaling data are visualized in Fig. ?? ADD REF. ADD A MENTION THAT THE NUMBERS FROM THE FIRST COLUMN REFERS TO THE QF FIGURE

Reaction number	Reaction	CN	Ref.	X_{mean}	BF
1	⁹³ Nb+ ⁹⁹ Ru	¹⁹² At	*	0.757	
2	$^{90}{ m Zr} + ^{103}{ m Rh}$	$^{193}\mathrm{At}$	[And23]	0.754	0.44
3	$^{51}V + ^{144}Sm$	$^{195}\mathrm{At}$	[And06b]	0.685	0.64
4	$^{54}\text{Fe} + ^{141}\text{Pr}$	$^{195}\mathrm{At}$	[Ket 03a]	0.715	0.64
5	56 Fe $+^{141}$ Pr	$^{197}\mathrm{At}$	[And16]	0.707	0.66
	56 Fe $+^{141}$ Pr		[Ket03a], [Ket03b]		0.66
6	$^{51}V + ^{147}Sm$	$^{198}\mathrm{At}$	[Nym13]	0.682	0.67
7	$^{40}\text{Ca} + ^{159}\text{Tb}$	$^{199}\mathrm{At}$	[Yer03]	0.672	0.76
8	$^{45}{\rm Sc} + ^{156}{\rm Gd}$	$^{201}\mathrm{At}$	[Wer15c]	0.668	0.65
9	$^{45}{\rm Sc} + ^{157}{\rm Gd}$	$^{202}\mathrm{At}$	[Wer15c]	0.667	0.70
10	$^{45}{\rm Sc} + ^{158}{\rm Gd}$	$^{203}\mathrm{At}$	[Wer15c]	0.666	0.71
11	$^{44}\text{Ca} + ^{159}\text{Tb}$	$^{203}\mathrm{At}$	[Wer15a]	0.654	0.69
12	$^{40}{\rm Ar} + ^{165}{\rm Ho}$	$^{205}\mathrm{At}$	[Ver 84]	0.632	0.79
	$^{40}{\rm Ar} + ^{165}{\rm Ho}$		[And 90]		0.79
	$^{40}{\rm Ar} + ^{165}{\rm Ho}$		[Jak10]		0.74
	$^{40}{\rm Ar} + ^{165}{\rm Ho}$		[Fol 12]		0.79
13	$^{24}{ m Mg} + ^{181}{ m Ta}$	$^{205}\mathrm{At}$	[And 90]	0.574	0.78
14	$^{26}{ m Mg} + ^{181}{ m Ta}$	$^{207}\mathrm{At}$	[Yer03]	0.561	0.81
15	$^{48}\text{Ca} + ^{159}\text{Tb}$	$^{207}\mathrm{At}$	[May14]	0.638	0.82
16	$^{52}{\rm Cr} + ^{144}{\rm Sm}$	$^{196}\mathrm{Rn}$	[And06a]	0.704	0.51
17	$^{56}{ m Fe} + ^{142}{ m Nd}$	$^{198}\mathrm{Rn}$	[Ket 01]	0.715	0.62
18	$^{52}{\rm Cr} + ^{147}{\rm Sm}$	$^{199}\mathrm{Rn}$	†	0.700	0.66
19	$^{82}{\rm Kr} + ^{118}{\rm Sn}$	$^{200}\mathrm{Rn}$	[And08]	0.746	0.67
20	$^{52}{\rm Cr} + ^{149}{\rm Sm}$	$^{201}\mathrm{Rn}$	†	0.697	0.68
21	$^{52}{\rm Cr} + ^{150}{\rm Sm}$	$^{202}\mathrm{Rn}$	†	0.696	0.68
22	$^{36}{\rm Ar} + ^{166}{\rm Er}$	$^{202}\mathrm{Rn}$	[Tay99]	0.658	0.74
23	$^{28}{ m Si}+^{176}{ m Hf}$	$^{204}\mathrm{Rn}$	[Tay96]	0.609	0.70
24	$^{44}\text{Ca} + ^{162}\text{Dy}$	$^{206}\mathrm{Rn}$	[Wer15b]	0.659	0.72
25	$^{48}\text{Ca} + ^{162}\text{Dy}$	$^{210}\mathrm{Rn}$	[May15]	0.643	0.74

 $^{^{\}ast}$ Reaction was recently measured at the Argonne National Laboratory - data not published yet

[†] Reactions analysed in this work

Table 4.5: Details of the experimental measurements at SHIP, where 186 Bi was produced.

Beam Target	CN	Beam energy [MeV]	Beam intensity [pnA]	Target thickness $[\mu \mathrm{g/cm^2}]$	Irradiation [h]
Exp1 ₉₅ Mo [And03]	$^{93}\mathrm{Nb}$ †	419, 438	10	900	36
Exp2 ${}^{46}\text{Ti}^{12+}$ [Lan13]	$^{144}\mathrm{SmF}_{3}$	239	150	300‡	70

^{*} Beam energy in front of the target

† Metallic target used

† The thickness of the compound target

Chapter 5

Summary

Conclusion

In this project, the results of the analysis of data collected in the reactions $^{95}\text{Mo}+^{93}\text{Nb} \rightarrow ^{188}\text{Bi}^*$ and $^{46}\text{Ti}+^{144}\text{Sm} \rightarrow ^{190}\text{Po}^*$, measured at the velocity filter SHIP, are presented. The former reaction was already investigated by Andreyev et al. in the α decay spectroscopic study of ^{186}Bi [And03], where γ transitions with energies of 108, 445 and 520 keV γ were assigned to the de-excitation of states populated by the α decay of the ^{186}Bi isomers. The merger of the datasets from the two reactions increased the total statistics three times in comparison to the referenced study. The analysis of prompt $\alpha - \gamma$ coincidences measured within $\Delta T(\alpha - \gamma) \leq 5\,\mu\text{s}$ allowed to conclusively assign (aside the transitions identified in the aforementioned study) 169 keV transition and tentative 97–132 keV γ cascade to the $^{186m1}\text{Bi}$. The 371 and 426 keV γ signals were assigned to the decay path of $^{186m2}\text{Bi}$. Other $\alpha - \gamma$ groups were difficult to decode and assign, due to the complex α distributions, reflecting the complicated structure of odd-odd isotopes.

An alternative approach by considering α +CE summing effects in α distributions was proposed and described. This analysis allowed to tentatively deduce the energy of the converted transition in cascade with a γ line, as well as its multipolarity. Gamma lines with energies of 186, 215, 238 and 255 keV were suggested to be in cascades originating from the 186m2 Bi, with tentatively deduced 285(M1), 195(M1), 175(M2) and 205(M1) keV transitions, respectively.

Outlook

A more proper analysis of the structure of 182 Tl would require significantly higher statistics and employment of an array of germanium γ detectors. In the studied reactions, the statistics of the γ lines in the region $E_{\gamma} \sim 200$ – $300\,\mathrm{keV}$ reached only up to few tens of collected signals and the complex α distributions suggest a complicated structure of 182 Tl. The detection efficiency of the germanium detector reaches roughly 5-10%, a reliable use of $\alpha - \gamma - \gamma$ coincident analysis would therefore require the production of 186 Bi in order of hundreds of thousands of produced nuclei. Another possibility would be the analysis of conversion electrons, which requires sufficiently low energy threshold of the particle detectors.

Cross section studies will require the analysis of several reactions leading to the radon and radium compound nuclei. Currently, data from the reactions $^{52}\text{Cr}+^{147,149,150}\text{Sm} \rightarrow ^{199,201,202}\text{Rn}^*$ and $^{56}\text{Fe}+^{147,149,154}\text{Sm} \rightarrow ^{203,205,210}\text{Ra}^*$ reactions measured at the SHIP at different beam energies are available. Each analysis will require the calibration of the detector setup, identification of the produced isotopes and evaluation of the corresponding cross sections. Further, the theoretical calculations of the cross sections with a use of statistical code HIVAP will be performed. The comparison of theoretical and experimental results and subsequent optimisation of the calculation parameters will yield the liquid-drop fission barrier scaling parameter and will help to extend the barrier scaling systematics known from the polonium and bismuth isotopes [And05]. Further comparison with other theoretical models, such as NRV (using channel coupling approach) [Kar16; Kar17] and PACE4 (implemented in LISE++ [Tar08]), would help to verify HIVAP calculations.

Appendices

Appendix A

Excitation functions for radon compound nuclei

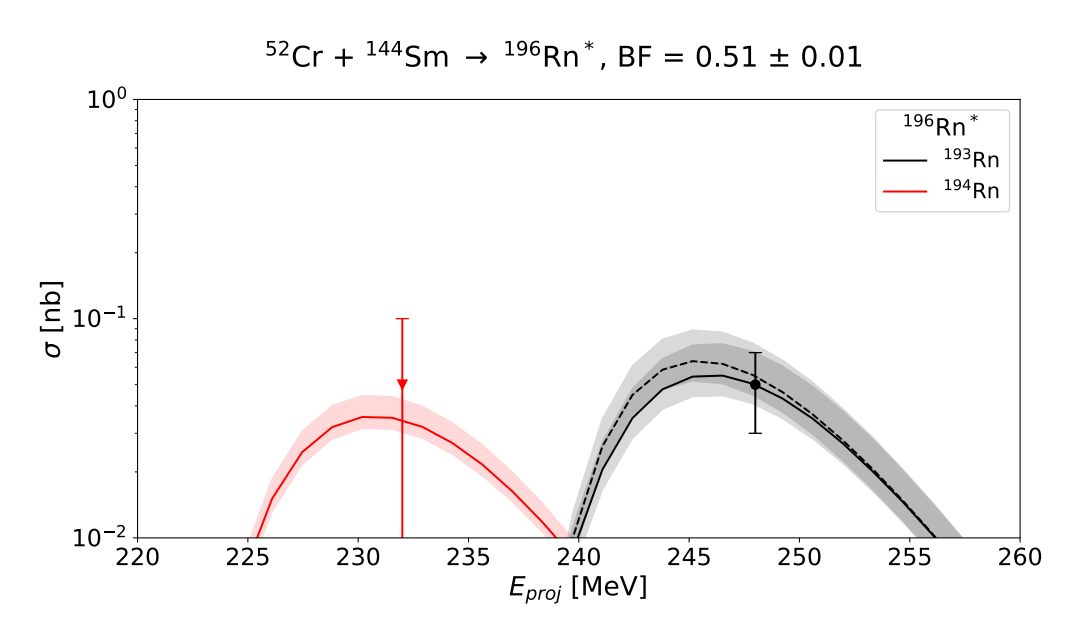


Figure A.1: The experimental (points) and theoretical (lines) excitation functions for the reaction $^{52}\text{Cr}+^{144}\text{Sm}\rightarrow^{196}\text{Rn}^*$. The solid lines denote the HIVAP calculations according to the BF approach, the dashed lines are for the IP parametrization, see Sec. 2.1.1. The matching semi-transparent shadow around the lines denotes the calculation with the BF±0.01 parameter. Experimental data are from [And06a].

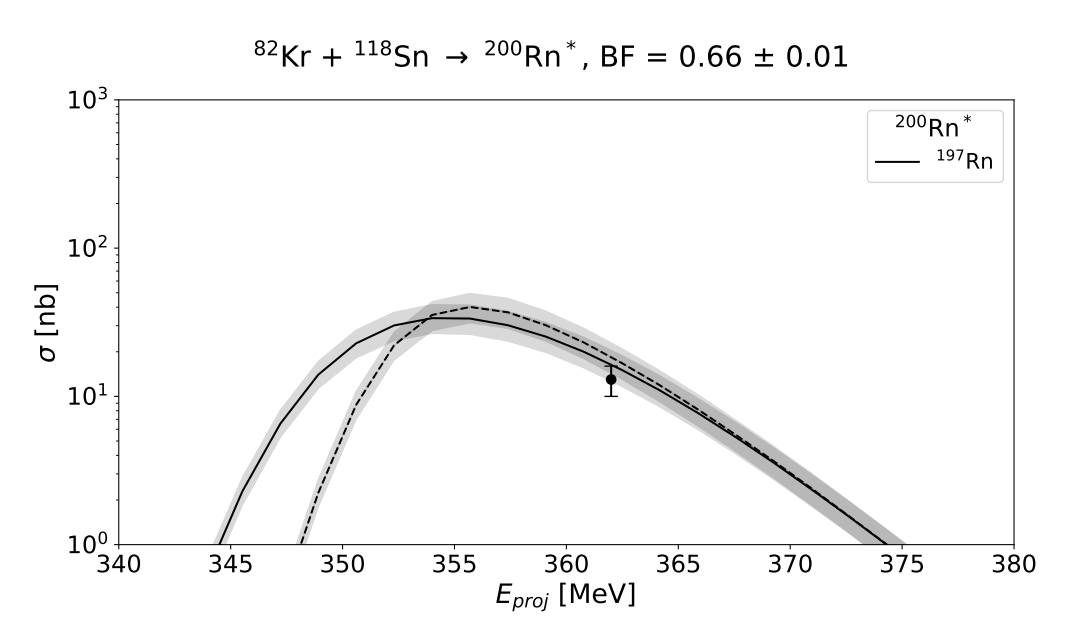


Figure A.2: The same as in Fig. A.1, but for the reaction $^{82}\text{Kr}+^{118}\text{Sn}\rightarrow^{200}\text{Rn}^*$. Experimental data are from [And08].

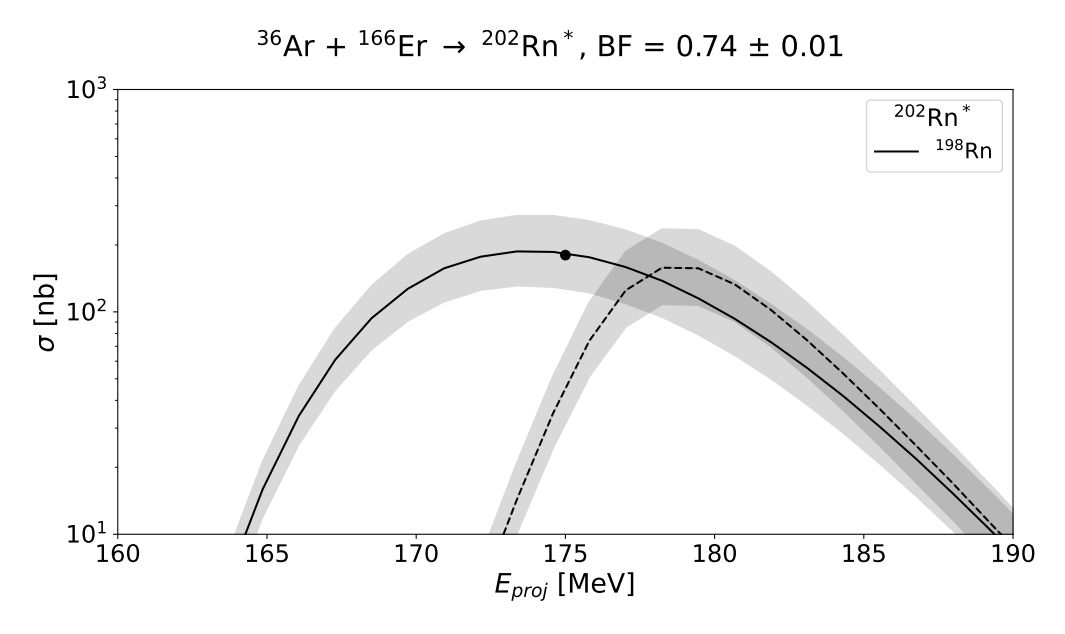


Figure A.3: The same as in Fig. A.1, but for the reaction $^{36}\mathrm{Ar}+^{166}\mathrm{Er}\rightarrow^{202}\mathrm{Rn}^*$. Experimental data are from [Tay99].

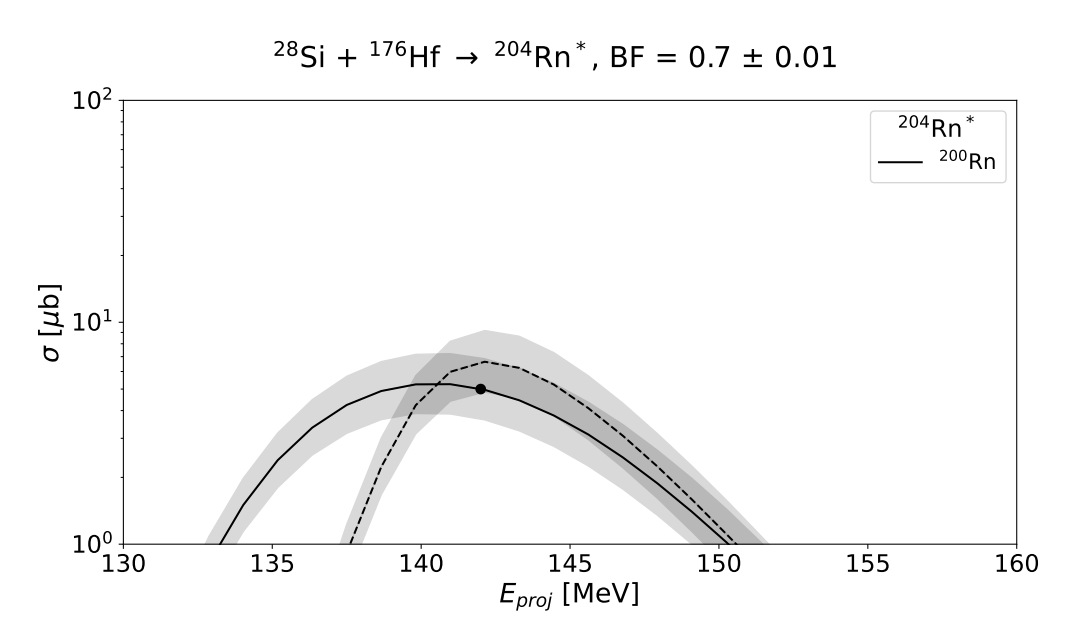


Figure A.4: The same as in Fig. A.1, but for the reaction $^{28}\text{Si}+^{176}\text{Hf}\rightarrow^{204}\text{Rn}^*$. Experimental data are from [Tay96].

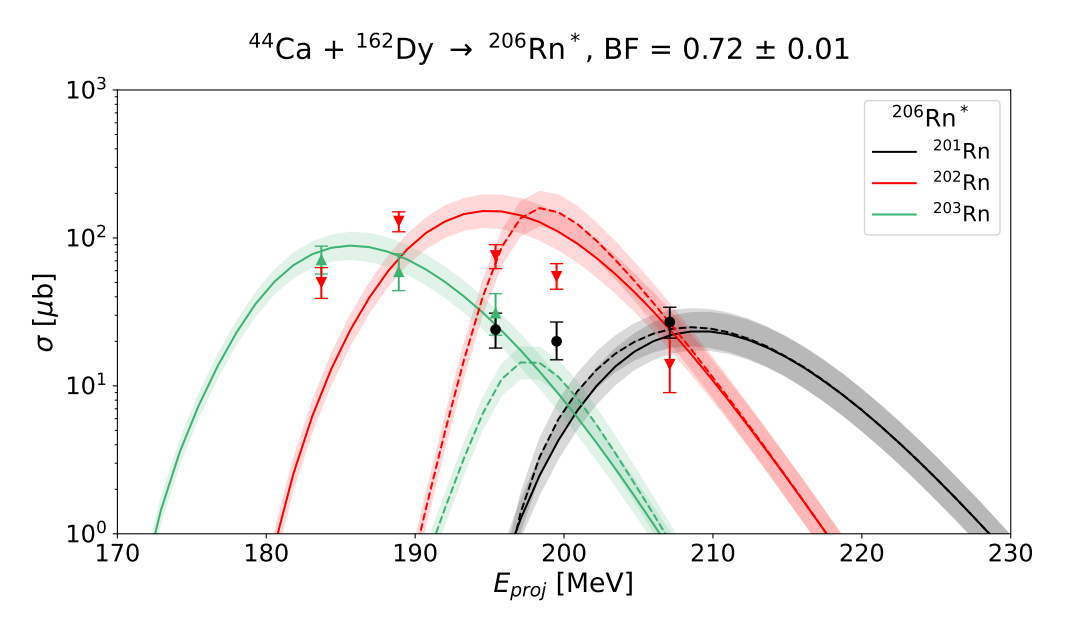


Figure A.5: The same as in Fig. A.1, but for the reaction $^{44}\text{Ca}+^{162}\text{Dy}\rightarrow^{206}\text{Rn}^*$. Experimental data are from [Wer15b].

Appendix B

Excitation functions for astatine compound nuclei

Bibliography

- [Ada08] J. Adamczewski-Musch, H. G. Essel, and S. Linev. Tech. rep. GSI Scientific Report, (2008).
- [Ala55] G. Alaga et al. In: *Mat. Fys. Medd. Dan. Vid. Selsk.* 29. (1955).
- [And00] A. N. Andreyev et al. In: *Nature* 405. (2000), p. 430. DOI: 10.1038/35013012.
- [And02] A. Andreyev et al. In: *Phys. Rev. C* 66. (2002), p. 014313. DOI: 10.1103/PhysRevC.66.014313.
- [And03] A. N. Andreyev et al. In: *Eur. Phys. J. A* 18. (2003), p. 55. DOI: 10.1140/epja/i2003-10051-1.
- [And05] A. N. Andreyev et al. In: *Phys. Rev. C* 72. (2005), p. 014612. DOI: 10.1103/PhysRevC.72.014612.
- [And06a] A. N. Andreyev et al. In: *Phys. Rev. C* 74. (2006), p. 064303.DOI: 10.1103/PhysRevC.74.064303.
- [And06b] A. N. Andreyev et al. In: *Phys. Rev. C* 73. (2006), p. 024317. DOI: 10.1103/PhysRevC.73.024317.
- [And08] K. Andgren et al. In: *Phys. Rev. C* 77. (2008), p. 054303. DOI: 10.1103/PhysRevC.77.054303.
- [And16] B. Andel. "Study of neutron-deficient polonium isotopes". PhD thesis.

 Comenius University in Bratislava, (2016).

 URL: https://alis.uniba.sk/storage/dpg/dostupne/FM/2016/2016-FM-43897/46176v1.
- [And23] A. N. Andreyev et al. In: *Phys. Rev. C* 108. (2023), p. 034303. DOI: 10.1103/PhysRevC.108.034303.
- [And90] A. N. Andreyev et al. In: Yadernaya Fizika 52. (1990). URL: https://www.osti.gov/etdeweb/biblio/5443016.

[Ant11] S. Antalic et al. In: Eur. Phys. J. A 47. (2011), p. 1. DOI: 10.1140/epja/i2011-11062-y.

- [Bas77] R. Bass. In: *Phys. Rev. Lett.* 39. (1977), p. 265. DOI: 10.1103/PhysRevLett.39.265.
- [Bas80] R. Bass. In: Deep-Inelastic and Fusion Reactions with Heavy Ions. Springer, 1980, p. 281.

 DOI: 10.1007/3-540-09965-4_23.
- [Bat97] J. C. Batchelder et al. In: Z. Phys. A 357. (1997), p. 121. DOI: 10.1007/s002180050223.
- [Boh36] N. Bohr. In: *Nature* 137. (1936), p. 344. DOI: 10.3367/UFNr.0016.193604a.0425.
- [Bru97] R. Brun and F. Rademakers. In: Nucl. Instrum. Methods A 389. (1997),
 p. 81.
 DOI: 10.1016/S0168-9002(97)00048-X.
- [Bur51] S. B. Burson et al. In: *Phys. Rev.* 83. (1951), p. 62. DOI: 10.1103/PhysRev.83.62.
- [Cal84] F. Calaprice et al. In: *Phys. Rev. C* 30. (1984). DOI: 10.1103/PhysRevC.30.1671.
- [Chu50] T. C. Chu. In: *Phys. Rev.* 79. (1950), p. 582. DOI: 10.1103/PhysRev.79.582.
- [Coh74] S. Cohen, F. Plasil, and W. J. Swiatecki. In: Annals of Physics 82. (1974),
 p. 557.
 DOI: 10.1016/0003-4916(74)90126-2.
- [Dra16] G. D. Dracoulis, P. M. Walker, and F. G. Kondev. In: Rep. Prog. Phys. 79. (2016), p. 076301.
 DOI: 10.1088/0034-4885/79/7/076301.
- [Enq96] T. Enqvist et al. In: Z. Phys. A 354 (1996), p. 9. DOI: 10.1007/s002180050005.
- [ENS24] ENSDF. Evaluated Nucelar Structure Data File. Accessed on March, 2024.

 URL: https://www.nndc.bnl.gov/ensdf/.
- [Fir96] R. B. Firestone and V. S. Shirley. "Table of Isotopes, 8th edition". Wiley, New York, (1996).

[Fol12] C. M. Folden III et al. In: Nucl. Instrum. Methods A 678 (2012), p. 1. DOI: 10.1016/j.nima.2012.02.035.

- [Fol95] H. Folger et al. In: Nucl. Instrum. Methods A 362. (1995), p. 64. DOI: 10.1016/0168-9002(95)00527-7.
- [Gam28] G. Gamow. In: Z. Phys. 51. (1928), p. 204. DOI: 10.1007/BF01343196.
- [Gei11] H. Geiger and J. M. Nuttall. In: The London, Edinburgh, and Dublin Philosophical Magazine and Journal of Science 22. (1911), p. 613. DOI: 10.1080/14786441008637156.
- [Ghi73] A. Ghiorso et al. In: *Phys. Rev. C* 7. (1973), p. 2032.DOI: 10.1103/PhysRevC.7.2032.
- [Gho50] S. N. Ghoshal. In: *Phys. Rev.* 80. (1950), p. 939. DOI: 10.1103/PhysRev.80.939.
- [Gro67] J. R. Grover and J. Gilat. In: *Phys. Rev.* 157. (1967), p. 802.DOI: 10.1103/PhysRev.157.802.
- [Gur28] R. W. Gurney and E. U. Condon. In: *Nature* 122. (1928), p. 439. DOI: 10.1038/122439a0.
- [Hah21] O. Hahn. In: *Die Naturwissenschaften* 9. (1921), p. 84. DOI: 10.1007/BF0149132.
- [Heß10] F. P. Heßberger et al. In: Eur. Phys. J. A 43. (2010), p. 55. DOI: 10.1140/epja/i2009-10899-9.
- [Hey83] K. Heyde et al. In: *Phys. Rep.* 102. (1983), p. 291. DOI: 10.1016/0370-1573(83)90085-6.
- [Hey87] K. Heyde et al. In: *Nucl. Phys. A* 466. (1987), p. 189. DOI: 10.1016/0375-9474(87)90439-8.
- [Hey88] K. Heyde et al. In: Nucl. Phys. A 484. (1988), p. 275.DOI: 10.1016/0375-9474(88)90073-5.
- [Hil53] D. L. Hill and J. A. Wheeler. In: *Phys. Rev.* 89. (1953), p. 1102.DOI: 10.1103/PhysRev.89.1102.
- [Hof00] S. Hofmann and G. Münzenberg. In: Rev. Mod. Phys 72. (2000), p. 733.
 DOI: 10.1103/RevModPhys.72.733.

[Hof79] S. Hofmann et al. In: Z. Phys. A 291. (1979), p. 53. DOI: 10.1016/0029-554X(79)90362-8.

- [Hul09] M. Hult et al. In: Applied Radiation and Isotopes 67. (2009), p. 918. DOI: 10.1016/j.apradiso.2009.01.057.
- [Ign75] A. V. Ignatyuk et al. In: Yad. Fiz. 21. (1975), p. 1185.
- [Jak10] U. Jakobsson et al. In: *Phys. Rev. C* 82. (2010), p. 044302. DOI: 10.1103/PhysRevC.82.044302.
- [Kar16] A. V. Karpov et al. In: Physics of Atomic Nuclei 79 (2016), p. 749.
 DOI: 10.1134/S1063778816040141.
- [Kar17] A. V. Karpov et al. In: *Nucl. Instrum. Methods A* 859 (2017), p. 112. DOI: 10.1016/j.nima.2017.01.069.
- [Kas98] M. Kaspar, J. Gerl, et al. Tech. rep. GSI-98-1, 195, (1998).
 URL: https://repository.gsi.de/record/53534.
- [Ket01] H. Kettunen et al. In: *Phys. Rev. C* 63. (2001), p. 044315.DOI: 10.1103/PhysRevC.63.044315.
- [Ket03a] H. Kettunen et al. In: Eur. Phys. J. A 17 (2003), p. 537. DOI: 10.1140/epja/i2002-10162-1.
- [Ket03b] H. Kettunen et al. In: Eur. Phys. J. A 16 (2003), p. 457. DOI: 10.1140/epja/i2002-10130-9.
- [Kib08] T. Kibedi et al. In: Nucl. Instrum. Methods A 589. (2008), p. 202. DOI: 10.1016/j.nima.2008.02.051.
- [Kin03] B. Kindler et al. In: AIP Conf. Proc. 680. American Institute of Physics.
 2003, p. 781.
 DOI: 10.1063/1.1619828.
- [Kin06] B. Kindler et al. In: *Nucl. Instrum. Methods A* 561. (2006), p. 107. DOI: 10.1016/j.nima.2005.12.232.
- [Kra88] K. S. Krane. "Introductory nuclear physics". John Wiley & Sons, (1988).
- [Kug00] E. Kugler. In: *Hyperfine interactions* 129. (2000), p. 23. DOI: 10.1023/A:1012603025802.
- [Kuz67a] V. I. Kuznetsov, N. K. Skobelev, and G. N. Flerov. In: Sov. J. Nucl. Phys 4. (1967), p. 202.

[Kuz67b] V. I. Kuznetsov, N. K. Skobelev, and G. N. Flerov. In: Sov. J. Nucl. Phys 5 (1967), p. 191.

- [Lan13] J. Lane et al. In: *Phys. Rev. C* 87. (2013), p. 014318. DOI: 10.1103/PhysRevC.87.014318.
- [Lom02] B. Lommel et al. In: *Nucl. Instrum. Methods A* 480. (2002), p. 16. DOI: 10.1016/S0168-9002(01)02041-1.
- [Lov06] W. D. Loveland, D. J. Morrissey, and G. T. Seaborg. "Modern Nuclear Chemistry." John Wiley & Sons, (2006).
- [Mar79] D. Marx et al. In: *Nucl. Instrum. Methods* 163. (1979), p. 15. DOI: 10.1016/0029-554X(79)90028-4.
- [May14] D. A. Mayorov et al. In: *Phys. Rev. C* 90. (2014), p. 024602. DOI: 10.1103/PhysRevC.90.024602.
- [May15] D. A. Mayorov et al. In: Phys. Rev. C 92. (2015), p. 054601.
 DOI: 10.1103/PhysRevC.92.054601.
- [Maz08] M. Mazzocco et al. In: *Nucl. Instrum. Methods B* 266. (2008), p. 3467. DOI: 10.1016/j.nimb.2008.04.017.
- [Möl16] P. Möller et al. In: At. Data. Nucl. Data Tables 109 (2016), p. 1.
 DOI: 10.1016/j.adt.2015.10.002.
- [Mor56] H. Morinaga. In: *Phys. Rev.* 101. (1956), p. 254. DOI: 10.1103/PhysRev.101.254.
- [Mos20] P. Mosat et al. In: *Phys. Rev. C* 101. (2020), p. 034310. DOI: 10.1103/PhysRevC.101.034310.
- [Mün79] G. Münzenberg et al. In: *Nucl. Instrum. Methods* 161. (1979), p. 65. DOI: 10.1016/0029-554X(79)90362-8.
- [Nym13] M. Nyman et al. In: *Phys. Rev. C* 88. (2013), p. 054320. DOI: 10.1103/PhysRevC.88.054320.
- [Poe06] D. N. Poenaru, I.-H. Plonski, and W. Greiner. In: *Phys. Rev. C* 74. (2006).DOI: 10.1103/PhysRevC.74.014312.
- [Poe80] D. N. Poenaru, M. Ivascu, and D. Mazilu. In: Journal de Physique Lettres 41. (1980), p. 589.
 DOI: 10.1051/jphyslet:019800041024058900.

[Pol62] S. M. Polikanov et al. In: Sov. Phys. – JETP 15. (1962), p. 1016.

- [Pop97] A. G. Popeko et al. In: Nucl. Instrum. Methods B 126. (1997), p. 294. DOI: 10.1016/S0168-583X(96)01094-4.
- [Pop99] A. G. Popeko et al. In: *Nucl. Instrum. Methods A* 427. (1999), p. 166. DOI: 10.1016/S0168-9002(98)01561-7.
- [Qi09] C. Qi et al. In: *Phys. Rev. C* 80. (2009). DOI: 10.1103/PhysRevC.80.044326.
- [Qui93] A. B. Quint et al. In: *Z. Phys. A* 346. (1993), p. 119. DOI: 10.1007/BF01294627.
- [Rac43] G. Racah. In: *Phys. Rev.* 63. (1943), p. 367. DOI: 10.1103/PhysRev.63.367.
- [Ras59] J. O. Rasmussen. In: *Phys. Rev.* 113. (1959), p. 1593. DOI: 10.1103/PhysRev.113.1593.
- [Rei81] W. Reisdorf. In: Z. Phys. A 300. (1981), p. 227.
 DOI: 10.1007/BF01412298.
- [Rei85] W. Reisdorf et al. In: *Nucl. Phys. A* 438. (1985), p. 212. DOI: 10.1016/0375-9474(85)90125-3.
- [Rei90] W. Reisdorf. HIVAP manual. Unpublished, (1990).
- [Rei92] W. Reisdorf and M. Schädel. In: Z. Phys. A 343. (1992), p. 47. DOI: 10.1007/BF01291597.
- [Rut11] E. Rutherford. In: The London, Edinburgh, and Dublin Philosophical Magazine and Journal of Science 21. (1911), p. 669.

 DOI: 10.1080/14786440508637080.
- [Šár96] Š. Šáro et al. In: Nucl. Instrum. Methods A 381. (1996), p. 520. DOI: 10.1016/S0168-9002(96)00651-1.
- [Sch84a] K.-H. Schmidt et al. In: *Z. Phys. A* 316. (1984), p. 19. DOI: 10.1007/BF01415656.
- [Sch84b] J. R. H. Schneider. Tech. rep. Unpublished, GSI-84-3, (1984).
- [Sie16] M. Siegbahn. In: *Nature* 96. (1916), p. 676.
- [Sod17] F. Soddy. In: *Nature* 99. (1917), p. 244. DOI: 10.1038/099244c0.

[Štr06] B. Štreicher. "Synthesis and spectroscopic properties of transfermium isotopes with $Z=105,\,106$ and 107". PhD thesis. FMFI UK, (2006).

- [Tan23] I. Tanihata, H. Toki, and T. Kajino. "Handbook of Nuclear Physics". Springer Singapore, (2023).
- [Tar08] O. B. Tarasov and D. Bazin. In: Nucl. Instrum. Methods B 266. (2008),
 p. 4657.
 DOI: 10.1016/j.nimb.2008.05.110.
- [Tay96] R. B. E. Taylor et al. In: *Phys. Rev. C* 54. (1996), p. 2926. DOI: 10.1103/PhysRevC.54.2926.
- [Tay99] R. B. E. Taylor et al. In: *Phys. Rev. C* 59. (1999), p. 673. DOI: 10.1103/PhysRevC.59.673.
- [Uus05] J. Uusitalo et al. In: *Phys. Rev. C* 71. (2005), p. 024306. DOI: 10.1103/PhysRevC.71.024306.
- [Van02] K. Van de Vel et al. In: *Phys. Rev. C* 65. (2002), p. 064301. DOI: 10.1103/PhysRevC.65.064301.
- [Van91] P. Van Duppen et al. In: *Nucl. Phys. A* 529. (1991), p. 268. DOI: 10.1016/0375-9474(91)90796-9.
- [Vaz81] L. C. Vaz, J. M. Alexander, and G. R. Satchler. In: *Phys. Rep.* 69. (1981),
 p. 373.
 DOI: 10.1016/0370-1573(81)90094-6.
- [Ver84] D. Vermeulen et al. In: Z. Phys. A 318 (1984), p. 157. DOI: 10.1007/BF01413464.
- [Wal20] P. Walker and Z. Podolyak. In: Phys. Scr. 95. (2020), p. 044004.
 DOI: 10.1088/1402-4896/ab635d.
- [Wau93] J. Wauters et al. In: *Physical Review C* 47. (1993), p. 1447. DOI: 10.1103/PhysRevC.47.1447.
- [Wei36] C. F. Weizsäcker. In: Naturwissenschaften 24. (1936), p. 813.
 DOI: 10.1007/BF01497732.
- [Wei40] V. F. Weisskopf and D. H. Ewing. In: *Phys. Rev.* 57. (1940), p. 472.DOI: 10.1103/PhysRev.57.472.
- [Wei51] V. F. Weisskopf. In: *Phys. Rev.* 83. (1951), p. 1073.DOI: 10.1103/PhysRev.83.1073.

[Wer15a] T. A. Werke et al. In: *Phys. Rev. C* 92. (2015), p. 054617. DOI: 10.1103/PhysRevC.92.054617.

- [Wer15b] T. A. Werke et al. In: *Phys. Rev. C* 92. (2015), p. 054617. DOI: 10.1103/PhysRevC.92.054617.
- [Wer15c] T. A. Werke et al. In: *Phys. Rev. C* 92. (2015), p. 034613. DOI: 10.1103/PhysRevC.92.034613.
- [Woo92] J. L. Wood et al. In: *Phys. Rep.* 215. (1992), p. 101. DOI: 10.1016/0370-1573(92)90095-H.
- [Yer03] A. V. Yeremin et al. In: *Physics of Atomic Nuclei* 66 (2003), p. 1042. DOI: 10.1134/1.1586416.

List of publications

Publications in current contents:

α decay of the neutron-deficient isotope ¹⁹⁰At
A. N. Andreyev, D. Seweryniak, B. Andel, S. Antalic, D. T. Doherty, A. Korichi, C. Barton, L. Canete, M. P. Carpenter, R. M. Clark, P. A. Copp, J. G. Cubiss, J. Heery, Y. Hrabar, H. Huang, T. Huang, V. Karayonchev, F. G. Kondev, T. Lauritsen, Z. Liu, G. Lotay, C. Müller-Gatermann, S. Nandi, C.

Page, D. H. Potterveld, P. H. Regan, W. Reviol, D. Rudolph, M. Siciliano, R.

S. Sidhu, A. Sitarčík, P. J. Woods, Z. Yue, and W. Zhang

Phys. Rev. C 108, 034303

DOI: 10.1103/PhysRevC.108.034303

